The Ediacaran Grenville dykes (SE Canada) reveal the weakest sustained palaeomagnetic field on record.

Daniele Thallner[1*], Andy Biggin[1], Henry Halls[2]

[1]Dept. of Earth, Ocean and Ecological Sciences, University of Liverpool, L69 3BX, UK

[2]Department of Earth Sciences, University of Toronto, 22 Russel Street, Toronto, Canada M5S 3B1

[*]Corresponding author:
Daniele Thallner
Email: daniele.thallner@liverpool.ac.uk
Address: Dept. Earth, Ocean and Ecological Sciences, University of Liverpool, L69 3BX, UK

Keywords: Paleointensity; Ediacaran; Laurentia; Grenville Dykes

Abstract

Long-term variations of the geomagnetic field, observed in the palaeomagnetic record, have the potential to shed much light on the evolution of Earth's deep interior. With a geomagnetic field characterised by anomalous directions and ultra-low intensities, the Ediacaran period (635-541 Ma) is a time of special interest. Steep and shallow directions, leading to virtual geomagnetic poles (VGPs), separated by angles of up to 90° and very close in age could have recorded a geomagnetic field switching between axial and equatorial dipole-dominated states. Alternatively, the field may simply have been highly nondipolar and subject to rapid reversals. Palaeointensity determinations of units that record the anomalous directions could potentially help to discriminate between morphologies but the spatial and temporal distribution of palaeomagnetic data require improvement. Here we present new palaeointensities from 11 sites from the western end of the Grenville Dyke swarm that recorded directionally anomalous geomagnetic fields around ~585 Ma. Palaeointensities, obtained through microwave Thellier, Shaw and pseudo-Thellier methods, show field strength values of 2.9±2.2 µT and corresponding virtual dipole moments of 0.3-1.7 x10^{22} Am^2. These field strengths are an order of magnitude weaker than the present-day field. The most extreme palaeointensity values of 1.4-2.1 µT are half as strong as seen in previous studies of the Ediacaran field and as low as Mars' recently measured crustal field intensity, giving a new lower bound for the Earth. VGPs grouping in two distinct clusters with almost identical angular dispersions of VGPs (S_B = 18.5° and 18.9°) may argue for the presence of an equatorial dipole. In contrast, the palaeointensities associated with the steep and shallow components are indistinguishable. This observation, together with the overall very large VGP dispersion may rather support that the Grenville Dykes have recorded enhanced secular variation linked to a highly unstable, multipolar and reversing field.

1. Introduction

Extreme climatic changes in the late Neoproterozoic (Evans and Raub, 2011) and tectonic activity between the final breakup of Rodinia and the assembly of Gondwana have made the Ediacaran period (542-635 Ma) a prime target for palaeomagnetic and geodynamic research. Especially the individual drifting histories of Laurentia and Baltica remain mysterious (Li et al., 2013) although both their positions are relatively well constrained around the beginning and the end of the Ediacaran at ~615 Ma and from ~550 Ma (e.g McCausland et al., 2007; Meert, 2014). Several sets of palaeomagnetic data are available to constrain the palaeogeography for Laurentia (e.g. Bono and Tarduno, 2014; McCausland et al., 2007; McCausland and Hodych, 1998) and Baltica (e.g. Bazhenov et al., 2016; Meert, 2014), but the resulting palaeopoles lead to ambiguous apparent polar wander paths (AWPW). Datasets from Laurentia and Baltica show both steep and shallow primary directional components that are extremely close in age. For Laurentia, both components were found in studies of the Sept-Îles intrusion (Bono and Tarduno, 2014; Tanczyk et al., 1987), the Grenville Dykes (Murthy, 1971, Halls et al., 2015) and the Catoctin Basalts (Meert et al., 1994). These components usually show dual-polarities and are often supported by field tests. The limitations imposed by the nature of a geocentric axial dipole field lead to discussions about which of the two components of each study could be less reliable and would not be used for the calculation of the APWP (e.g. Bono and Tarduno, 2014; McCausland et al., 2007; Robert et al., 2017). Depending on which of the seemingly primary components are rejected, high plate motion velocities are required to allow the latitudinal changes in the resulting APWPs which lead to different theories explaining the geodynamic processes in the Ediacaran, including inertial interchange true polar wander (Kirschvink et al., 1997). In more recent studies, the puzzling APWPs have been attributed to anomalous directional behaviour of the geomagnetic field itself. Specifically, the steep and shallow directions have been interpreted as being caused by the geomagnetic field flipping between an axial and an equatorial dipole field configuration (Abrajevitch and Van der Voo, 2010) or as showing an intermediary state of an axial dipole field during continuous reversals (Halls et al., 2015). Numerical geodynamo simulations have suggested that the occurrence of a protracted equatorial dipole field may be possible during the reversal of an axial dipole field (Aubert and Wicht, 2004; Gissinger et al., 2012) with significant differences between the intensities of the axial and equatorial field states. Studies of magnetostratigraphic data from the late Ediacaran and the early-mid Cambrian (Bazhenov et al., 2016), resulting in reversal frequencies of more than 20 reversals/ Ma, claim that the field might have been in a hyperactive state at that time. Due to the correlation between reversal frequency and dipole field strength (Kulakov et al., 2019; Tauxe et al., 2013) the dipole field strength in the Ediacaran is expected to be low. First palaeointensity studies of Ediacaran rocks from Canada (Bono et al., 2019) and Ukraine (Shcherbakova et al., 2020) show ultra-low virtual dipole moments (VDM) that are an order of magnitude weaker than dipole moments in the Phanerozoic. To date, similarly low dipole moments have only been found in the Devonian (Hawkins et al., 2019; Shcherbakova et al., 2017) and the Jurassic (Kulakov et al., 2019; Tauxe et al., 2013). Information about reversals and palaeointensities are critical to delineate the anomalous field behaviour in the Ediacaran. However, no estimates for the strength of the geomagnetic field exist for the early-mid Ediacaran before 580 Ma. Here we report multi-method palaeointensity measurements performed on mid-Ediacaran age units showing both steep and shallow directions to look for differences that could help explain the directional observations of that time.

2. Materials and methods

2.1. **Sample material:**

The samples from dykes within the Grenville province used in this study were those collected for the study of Halls et al. (2015) and were taken preferentially from chilled margins. Several dykes were sampled at multiple sites over distances of up to 150 km. Analysis of geochemical composition helped with longitudinal correlation of the dykes. Samples were selected for intensity determination if sister-samples from the same site showed a stable component of ChRM in the previous study, which was the case for 99 samples from 15 sites within nine dykes (Figure 1). Following the naming convention used in Halls et al. (2015), the five dykes analysed in this study were: Coniston dyke (sites GD02, GD33), French River dyke (site GD23), Key River dyke (sites GD10, GD15, GD16, GD19, GD37) and Sand Bay dyke (site GD29). Additionally, four sites from other dykes in the area associated with the dyke swarm (sites GD07, GD25, GD26, GD30) were also analysed. U-Pb ages exist for Sand Bay dyke (585.2±0.8 Ma), Augusta Lake dyke (584±0.6 Ma), Key River dyke (587.3±0.7 Ma and French River dyke (598.0±1.4 Ma).

Distances between sites of the same dyke were generally larger than 2km and the sites were therefore regarded as separate spot readings of the field strength for the purpose of this study. Differences in chemical composition between the individual dykes suggest single intrusion events at different development stages of the magma chamber (Halls et al., 2015). The directional results in Halls et al. (2015) show four components resulting in antipodal steep and shallow directions close to directions of older studies of the Grenville dykes (Hyodo and Dunlop, 1993; Murthy, 1971). Positive contact (Halls et al., 2015) and reversal tests (Hyodo and Dunlop, 1993) support the primary nature of the steep direction. This comprises components B and E, that can be seen in sites of the Key River dyke (Halls et al., 2015) which are close to the directions recorded by the Mattawa dyke (585.9 Ma, Hyodo and Dunlop, 1993). The shallow component from the almost antipolar components C and D can also be observed continuously in sites of the same dyke and component D differs significantly from the regional overprint recorded in the close-by Whitestone anorthosite (Ueno et al., 1975). Because of an inconclusive contact test, it cannot be excluded that this component was remagnetised (Halls et al., 2015; Robert et al., 2017). In this study, we nevertheless analysed samples from sites that recorded both steep and shallow components.

2.2 Methods:

All measurements were carried out at University of Liverpool's Geomagnetism Laboratory. At least one specimen per site was selected for rock magnetic measurements. Measurements of IRM, hysteresis parameters and thermomagnetic curves were done on a Variable Field Translation Balance (VFTB) using both crushed specimens and cylinder specimens with a diameter of 5 mm. Additionally, temperature dependent susceptibilities were measured on an AGICO MFK-1A Kappabridge using crushed specimens heated in air to 700°C. To monitor thermochemical alterations in more detail, the same measurements were also performed in incremental heating and cooling cycles in temperature steps of 100°C between 150°C and 650°C. Scanning electron microscope (SEM) images were taken with a Hitachi TM3000 tabletop microscope and analysed with Quantax70.

The magnetic viscosity of 59 specimens was determined by measuring their remanent magnetisation after being stored for three weeks in different orientations without shielding from the ambient field (Prévot, 1981). For this experiment, the specimens were stored on a rack in the laboratory with their z axis parallel to the field lines of the geomagnetic field for the first duration and antiparallel to the field lines for the second duration. The remanent magnetisations were measured on an AGICO JR6 spinner magnetometer.

Four different methods were used to acquire palaeointensity data:

Microwave Thellier type palaeointensity experiments were performed on the high frequency (14GHz) microwave system and SQUID magnetometer (Hill and Shaw, 1999). This instrument uses cylinder specimens with a 5mm diameter. These were drilled from the available 1" cylinders, which allowed for 5 to 15 sub-specimens to be drilled from one standard cylinder specimen. Specimens are subjected to microwave treatment with incrementally increasing power and/or duration in a range between 20W.s and 500 W.s. The succession of zero-field (Z) and in-field (I) steps for the experiments followed the IZZI protocol (Tauxe and Staudigel, 2004). A pTRM-check was done after every other I-Z-pair, resulting in 4-5 pTRM-checks per specimen. To detect multidomain effects, the laboratory field was applied in angles of 45°-90° to the ChRM of the specimen (Yu and Tauxe, 2005). The laboratory field itself was varied between 3 and 30 μT between experiments to detect possible field dependencies of the results.

Thermal Thellier experiments were undertaken using the IZZI protocol with pTRM checks in vacuum, using an MMTD80 oven with a bias field of 10 μT in the temperature range of 100°C-550°C. Magnetisations of the specimens were measured on an AGICO JR6 spinner magnetometer after being 'cleaned' with a 2 mT AF step before every measurement using an AGICO LDA5 AF demagnetiser.

The double-heating Shaw method of (Tsunakawa and Shaw, 1994) used AF demagnetisations and ARM acquisitions carried out on a 2G RAPID superconducting rock magnetometer system in incremental steps of 2-10 mT up to a peak AF-field of 100 mT. ARMs were given at peak AF-field in bias fields of 57.9 μT or 81.2 μT. The specimens were given a full TRM twice by heating them to 610° or 650°C in bias fields of 5 μT or 10 μT to be able to apply an ARM correction (Rolph and Shaw, 1985).

The pseudo-Thellier method (Paterson et al., 2016; Tauxe et al., 1995) was performed on the automatic 2G RAPID system with the same AF levels as used in the Shaw method. This was done to have results that avoided heating the specimen at all during palaeointensity determination but its results were only used to confirm the results from the other methods. For the purpose of this experiment, bias fields of 11.4 μT and 81.2 μT were used for the ARM acquisition and, in some cases, Shaw and pseudo-Thellier experiments were run as a combined experiment, where the ARM acquisition steps were performed between the NRM0 and ARM0 steps of the Shaw experiments.

Different sets of selection criteria have been used to assess the quality of the palaeointensity experiments using the different methods.

For all Thellier-type experiments, the selection criteria followed the Standard Palaeointensity Definition (SPD, (Paterson et al., 2014) and were modified from the SELCRIT2 criteria (Biggin et al., 2007). The criteria of N=4, FRAC ≥ 0.35, ß ≤ 0.1, q ≥ 1, MAD ≤ 15°, α ≤ 15°, DRAT ≤ 10% and CDRAT ≤ 10% were used together with a curvature factor if the best-fit line (Paterson, 2011) of |k'| ≤ 0.48.

The selection criteria used for the Shaw method were similar to those set out by Yamamoto et al., (2010),: number of consecutive data points N ≥ 5, correlation coefficients of the linear parts of the NRM-TRM1* diagram and the TRM1-TRM2* diagram of $r^2_N \geq 0.995$ and $r^2_T \geq 0.995$, the fraction of used NRM f ≥ 0.2 and the slope of the linear part of the TRM1-TRM2* diagram $0.95 \leq \text{slope}_T \leq 1.05$. In addition, the selected part of the NRM must appear convergent on the orthographic plot of the NRM demagnetisation with α and MAD values ≤ 10°.

The SPD selection criteria used for pseudo-Thellier experiments were slightly relaxed from Paterson et al., (2016) and applied to a convergent part of NRM in the orthographic plot: N ≥ 6, f ≥ 0.3, ß ≤ 0.1, $r^2\text{corr} \geq 0.990$, $f_{\text{resid}} \leq 0.15$, α ≤ 10°, MAD ≤ 10°, |k'| ≤ 0.27 and $0.85 \leq |b_{AA}| \leq 1.15$.

Results that passed all criteria were classified as ‘class A’ result. We found that by relaxing a single criterion to a less strict value, we could dramatically increase success rates without severely affecting the overall result quality. Results that required a single criterion to be relaxed were classified as ‘class B’ results. Limits for relaxed selection criteria were: FRAC ≥ 0.25, DRAT ≤ 15% or CDRAT ≤ 15% for Thellier-type experiments and $r^2_N \geq 0.990$, $r^2_T \geq 0.990$ or $0.90 \leq \text{slope}_T \leq 1.10$ for Shaw experiments. If more than one criterion would have to be relaxed for a result to pass, the estimate was rejected.

3 Results

Thermomagnetic curves and susceptibility versus temperature curves measured on samples from different dykes showed quite diverse behaviour (supplementary figure 1). Most specimens showed one or two Curie temperatures between 550°C and 580°C. Specimens from the French River and Key River dykes as well as specimens from sites GD25 and GD26 also had noticeable Hopkinson peaks, indicating fine magnetite. Exceptions were measurements on specimens from site GD01 with a Curie temperature of 470°C and from sites GD07 and GD30, where susceptibilities were about two orders of magnitude weaker. With the exception of these specimens and those from Coniston dyke (GD01) and site GD33 of Augusta Lake dyke, thermomagnetic curves were mostly reversible. The susceptibility curves of specimens from Coniston (GD01, 14), French River (GD23) and Sand Bay (GD29) dykes showed a small ‘toe’ with another Curie temperature up to 610-620°C, possibly suggesting the presence of a small fraction of maghemite or titanohematite. Backscattered electron imaging (figure 2a-c) shows mostly relatively fresh coarse (~30-200 μm) (Ti-)magnetite grains with sharp edges as well as small dendritic (< ~40 μm) TM grains (e.g. figure 2a,b), indicating rapid cooling of the rocks. EDS elemental composition mapping of larger grains shows structures of full and partial exsolutions with lamellae of titanium rich ilmenite and titanium poor magnetite (figure 2c, supplementary figure 2). The preservation of high temperature textures and lack of low-temperature oxidation structures suggest that the grains are carriers of a primary TRM. For some samples it cannot be ruled out that the oxy-exsolution continued to temperatures lower than the Curie temperatures, but this has shown to only have small effects on the resulting palaeointensities (Shcherbakov et al., 2019).

Hysteresis parameters, shown in Figure 2e) and f), fall in two clusters on the Day et al., (1977) plot with one large cluster in the "PSD" area and another cluster with higher Bcr/Bc ratios. Most specimens plot close to the TM0 line (Wang and Van der Voo, 2004). This includes results from the French River dyke, which showed a substantially higher TiO_2 content in the geochemical analysis of the sites in Halls et al. (2015). In contrast, specimens from the low-Ti-type Coniston dyke (Halls et al., 2015) plot further away from the TM0 and closer to the TM60 line.

Fractions of viscous remanent magnetisations (VRM) of specimens from the different sites, acquired after 3 weeks in the ambient field, did not show any differences at the dyke level. The average viscosity index (v) for all sites (figure 2 d) was 14.4% (median = 9.6%, standard deviation = 14.9%). This mean viscosity index includes v values of up to 80% from sites GD07 and GD30. Specimens from those sites were basically non-magnetic and the viscosity index was mostly calculated from noise. Specimens with v values of >30% were not used for intensity determination. We note that low palaeointensities will naturally produce weak NRMs which will then be more radically affected by a VRM acquired in the strong present-day field.

Results of palaeointensity experiments are summarised in table 1. The total number of Shaw experiments only accounts for specimens that were retained for the full routine. The experiment was stopped after the first demagnetisation series (NRM0) for 16 specimens whose ChRM could not be isolated. Microwave demagnetisation experiments were performed on 29 sister specimens to determine their response to microwave treatments. Specimens from the same core as specimens that did not respond well to the microwave treatment during demagnetisation, or were too weak to be demagnetised at all, were not used for intensity experiments with the microwave Thellier method. In total, palaeointensity measurement was attempted on 189 specimens of the Grenville dykes. Of these, 128 (68%) used microwave IZZI, 20 (11%) used thermal IZZI, and 41 (21%) used Shaw and/or pseudo-Thellier experiments (Table 1).

Specimens universally showed non-ideal behaviour during thermal Thellier experiments. These mostly resulted in chaotic Arai and orthographic plots (figure 3e) and the experiment was stopped at 550°C. Strong 'zig-zagging' and high β values suggest strong MD behaviour over the full temperature range. In contrast, pTRM checks passed the criteria up to the highest temperature steps.

The majority of Arai plots from all Thellier experiments (75%) and of passing Thellier results (94%) showed two slopes as illustrated in figure 3. Similar to the results of other studies yielding extremely low palaeointensities (Hawkins et al., 2019; Shcherbakova et al., 2020), the sharp bend between the high and low temperature/power slopes usually coincided with the junction between ChRM and secondary components in the associated Zijderveld plots (figure3 a,c), but this is was not clearly visible for all results (figure 3 b). Of the accepted microwave Thellier type results, 10 passed as class A and 15 as class B result. For all class B results, either DRAT or CDRAT (but not both) had to be relaxed. About 10% of the results that were not accepted failed only one of the selection criteria. All other non-accepted results failed more than one selection criterion (e.g. figure 3e). The most commonly failed criteria were β (57% of results), FRAC (56%) and DRAT/CDRAT (48/52%). The high failure rate due to β and DRAT/CDRAT shows that MD effects and mineral alterations during heatings were both primary issues in the results of thermal and microwave experiments. Of the low temperature/power slopes, 6 results (5%) would pass the selection criteria, but it is clearly visible in the orthographic plot that the selected fraction is not the ChRM (figure 3d). One outlier intensity from a high-power slope of 26.7 µT was rejected as unreliable even though the result passed the selection criteria (GD19-43B1). Here, sister specimens from the same 1” core gave inconsistent intensities ranging from 3.6 to 140 µT.

Of the 12 accepted Shaw results, 7 passed as class A and 5 as class B results. For all 7 class B results, the correlation coefficient of the best fit line in the NRM-TRM1* plot r^2_N was relaxed to $r^2_N \geq 0.990$ (figure 4a). Results not passing r^2_N and/or slope_T was the main reason for unsuccessful experiments. Specimens showed a wide range of coercivities with a mean MDF = 19.2 ±9.6 mT. Secondary magnetisations that accounted for NRM fractions of up to 80% were usually removed by AF fields of less than 40 mT. Similar to the AF demagnetisation experiments in Halls et al. (2015), that successfully generated reliable directions and passed field tests, the remaining fraction of primary NRM was large enough in the Shaw experiments as well so that only two specimens failed the FRAC criterion.

From the 7 pseudo-Thellier and the 21 Shaw/pseudo-Thellier experiments 5 pseudo-Thellier results passed selection criteria and were accepted. Due to the high uncertainty of pseudo-

Thellier intensities associated with the used calibration factor (Paterson et al., 2016), the resulting palaeointensities were not considered in the calculation of the mean palaeointensities. However, since thermal alteration of the specimens during experiments was one of the main issues in the other methods, the pseudo-Thellier results can be useful to confirm that the results from the other methods are not biased by such alterations. Results from successful pseudo-Thellier experiments showed good agreement with the site mean values calculated from microwave and Shaw results (Table 1) with the mean values of sites GD33, GD29 and GD26 being within the 25% uncertainty range of the associated pseudo-Thellier results. For sites GD26 and GD37 that show a larger difference (>1 µT) between intensities from pseudo-Thellier experiments and intensities from other methods, the palaeointensities from pseudo-Thellier experiments are lower than the palaeointensities from the other methods. Most of the unsuccessful pseudo-Thellier experiments failed due to a high curvature of the selected line segment in the demag-demag plot (figure 4b), suggesting that NRM and ARM (de)magnetisations behave differently in these specimens and a palaeointensity calculated from these would be unreliable.

Combining class A and class B results, 25 results of the microwave Thellier experiments (20% success rate) and 12 results of the Shaw experiments (35%) passed the used selection criteria. No result of the thermal Thellier experiments passed selection criteria, leading to an overall success rate of 20% for Shaw and Thellier-type experiments. Palaeointensity estimates were averaged for each site as separate spot readings of the field strength (Table 1). The resulting intensity values range from 1.4 µT to 7.6 µT, and yielded virtual dipole moments (VDM) from 0.3 to 1.7 $*10^{22}$ Am^2. Five pseudo-Thellier results passed selection criteria as well and gave intensity values between 1.1 µT and 4.1 µT. All intensity results with critical values are listed in supplementary tables 1-3 and measurement data of all intensity experiments are available on the MagIC database (www2.earthref.org/MagIC).

4 Discussion

The geomagnetic field in the Ediacaran is characterised by ambiguous field directions that impede the construction of reliable APW paths. Recently, it has been stated that the time averaged dipole field strength is uniquely low in the Ediacaran (Bono et al., 2019) which is supported by the only other palaeointensity study of Ediacaran rocks to date (Shcherbakova et al., 2020). We expand the intensity data from these studies with the whole rock palaeointensities of the Grenville dykes with virtual dipole moments between 0.3 $*10^{22}Am^2$ and 1.7 $*10^{22}Am^2$.

Due to the low number of available samples and non-ideal behaviour during thermal Thellier experiments, microwave experiments were preferred as the small sample size allowed for a high number of experiments with sub-specimens. To account for a possible method-bias of the MW results, a number of thermal Thellier, Shaw and pseudo Thellier experiments were conducted as well. All methods suffered from low success rates that made it hard to compare the different methods on the site level. Where such a comparison was possible, the results from different methods differed by less than 1 µT, similar to the overall intensity variability on the dyke level. From this, a method related systematic bias seems unlikely. Furthermore, results from Thellier and Shaw experiments are also supported by the results of the pseudo-Thellier experiments.

To confirm that the intensity results are not biased by the choice of selection criteria, other commonly used sets of selection criteria have been used to re-analyse all Thellier-type results.

Accepted results from the different sets of criteria have been compared (supplementary table 4). All sets show only small differences in the range of ~1 µT and agree well with the results of the Shaw experiments. Supplementary table 4 also shows that results from combining class A and class B results only differ from pure class A results by 0.2 µT and are well inside the standard deviation of class A results, while the number of accepted results almost doubled.

The two-slope behaviour, seen in most Arai plots of Thellier experiments in this study, has been recognised in other studies of basalts with low palaeointensities as well (Hawkins et al., 2019; Kodama et al., 2019). Similar behaviour is often connected to MD behaviour (Riisager and Riisager, 2001; Smirnov et al., 2017) and/or alteration of magnetic minerals during heating steps of the experiments (Kissel and Laj, 2004) as well as to instabilities of aged thermoremanence (Shaar and Tauxe, 2015). Thermochemical alteration during the heatings was very common in the experiments of this study and results that were affected by alteration, as seen from pTRM checks, were not accepted. Curved or zig-zagging Arai plots, caused by MD behaviour and/or instability of TRM have been excluded as well if the curvature or β criteria were not met. Hawkins et al. (2019) argued that the two-slope behaviour without a corresponding directional change in their study was attributed to strong thermal or thermoviscous overprints of similar direction. This is also the case in our study, but here a directional change is often observable at the bend between the two slopes in the Arai plots as well. Therefore, the slope of the high unblocking temperature ranges, that also carried the ChRM in Halls et al. (2015), have been selected in the Arai plots to calculate palaeointensities.

The overall reliability of palaeointensity results was quantified by the application of Q_{PI} criteria (Biggin and Paterson, 2014) to each of the sites (see supplementary table 5).

The AGE criterion was met by all sites in the dykes dated in Halls et al. (2015). Sites GD33 from Augusta Lake dyke and site GD29 from Sand bay dyke were the only sites to meet the STAT criterion. The site GD23 from French River dyke has more than the minimum of 5 individual intensity estimates, but the estimate had a dispersion (standard deviation/mean) ≤ 25% (Paterson et al., 2010), which is often the case for ultra-low palaeointensity results (e.g. Hawkins et al., 2019; Shcherbakova et al., 2020). All other sides yielded less than the 5 successful palaeointensity results needed to meet the STAT criterion.

Mostly fresh looking titanomagnetite grains with high temperature oxy-exsolution structures and rapidly cooled dendritic magnetite grains without signs of low-temperature oxidations as seen from SEM suggest that the magnetisation is a primary TRM. However, concerns can be raised about the validity of the magnetisation itself due to the anomalous nature of the palaeodirections (Halls et al., 2015). This is especially the case for sites associated with the shallow directional component where the possibility of a remagnetisation event cannot be completely dismissed due to inconsistent results of a baked contact test (Robert et al., 2017). Halls et al. (2015) argued that these directions are also primary because they are almost antipodal and can be followed continuously along the dyke. Palaeointensity estimates, irrespective of the associated directions were similar and extremely low and the angular dispersions of VGPs show almost identical behaviour of steep and shallow components. On the basis of the combined microscopic and palaeomagnetic evidence, we chose to award the TRM criterion to all sites.

The use of pTRM checks and the application of the IZZI protocol with β and k’ criteria as well as the double heating checks of the Shaw experiments enabled the exclusion of all estimates that could be significantly biased by thermochemical alteration or MD behaviour during the experiments. Therefore, all sites passed both the ALT and MD criteria. Following the standard palaeointensity definitions 1.1 (Paterson et al., 2014), the angle between the laboratory field and the last pTRM check of the Thellier experiments was calculated as γ = 3.2°±1.2°, showing that the results were not majorly influenced by anisotropy effects. Systematic bias of estimates due to non-linear TRM behaviour was avoided by using different laboratory TRM fields between 3 µT and 30 µT and ARM fields between 10 µT and 81.2 µT. The similarity of results between the Shaw method with cooling times of ~1h and the microwave Thellier method with cooling times in the order of a fraction of a minute exclude a cooling rate bias. Therefore, the ACN criterion was given to all sites.

Four different methods were used to determine palaeointensities. To pass the TECH criterion, the palaeointensity estimate of a unit has to comprise results from at least two different methods and this was the case for 4 sites (supplementary table 5). The criterion LITH was only awarded to site GD37 since it combines results from both the dyke and baked host rocks. It was not met by any of the other sites as all intensity estimates came from the same lithology. Results of all intensity experiments with critical values are available in supplementary tables 1-3. In addition, all intensity measurement data is available on the MagIC database, which awards the MAG criterion to all units.

Summing up the QPI criteria results in scores of 6-8, showing that the palaeointensity estimates in this study are of high quality. This allows the palaeointensities associated with the steep B and shallow C+D directions found in Halls et al. (2015) to be compared. Averaging site mean palaeointensities of all sites with shallow directions results in 3.7 ±2.3 µT whereas the average palaeointensity of sites with steep directions gives 5.0 ± 0.5 µT. Assuming a high-latitude Laurentia around ~590 Ma, the palaeointensities of the shallow component – if recording an equatorial dipole field state – might be expected to be much lower than the intensities of the steep component. The average intensities of sites with the shallow component are indeed weaker, but with the higher values being within one standard deviation of the weaker values, the difference of < 2 µT is negligible. The similarity of the ultra-low palaeointensities of the two components suggests that the Grenville Dykes have recorded a highly unstable field as proposed in Halls et al. (2015). In contrast, the high and almost identical values for angular dispersions (supplementary figure 3) of two distinct groups of VGPs around the mean VGPs of the steep (S_B=18.5°) and the shallow component (S_B=18.9°) look consistent with the existence of an equatorial dipole. However, some caution is advised when taking the dispersions at face value. Previous studies of VGP scatter required a minimum of N = 9 sites (Doubrovine et al., 2019; Veikkolainen and Pesonen, 2014). Due to the exclusion of lower quality directions from sites with n ≤ 4 or k ≤ 30 in the calculations, this requirement was only met by the shallow component (N = 11), but not by the steep (N = 7). The dispersion values seem reasonable for the time period with comparable values for Laurentia showing a wide range between S_B = 13.5° (Skinner Cove volcanics, McCausland and Hodych, 1998; Veikkolainen and Pesonen, 2014) and S = ~26° (Sept-Îles intrusion, Bono et al., 2019). If the two groups of VGPs were interpreted as one group, showing a transitional field, then the resulting VGP dispersion would be S_B = 32.4° (variable cutoff = 63.4°) at low latitude. This would be an extremely high value but the current lack of constraints on the Ediacaran field means that it is not implausible.

With the exception of sites GD14 and GD25, where single high (7.6 and 12.6 µT) microwave results lead to high VDMs of 1.7 $*10^{22}Am^2$, the site mean VDMs of 0.3 - 0.9 $*10^{22}Am^2$ are comparable to, but lower than, the results of the Sept Iles (Bono et al., 2019) and the Volyn Traps (Shcherbakova et al., 2020) with corresponding VDMs of 0.5 and 1.0 $*10^{22}Am^2$. They therefore define a new lower boundary for the field strength in the Ediacaran. The palaeointensities, coming from dykes with ages that span ~15 Ma, suggest a sustained geomagnetic field with these extremely low intensities. These results are an order of magnitude weaker than the strength of the present-day field and the average palaeointensities of site GD26 and sites from the French River dyke and the Augusta Lake dyke with values between 1.4 and 2.1 µT are even as low as recent measurements of Mars' crustal field made by the InSight lander of ~2 µT (Johnson et al., 2020). Palaeointensities this low have been reported for Earth before, but were generally not attributed to a sustained field. The PINT database (Biggin et al., 2015) contains 6 site mean estimates with H_{pal} ≤ 5 µT or VDM ≤ 0.5 $*10^{22}$Am^2, N > 1 and reliable experiment types (excluding single-heating Shaw and total TRM experiments) that can be roughly divided into two groups. The first group comprises entries with mid-Miocene or younger ages that show the ultra-low intensity values in single basalt flows from Iceland (Lawley, 1970) and the Canary Islands (Brown et al., 2009; Leonhardt and Soffel, 2002) that are all connected to the short-term drop of dipole moments during polarity transitions interrupting a much stronger sustained field. The palaeointensities with Mesoproterozoic to Archaean ages from the second group are either extremely low due to fractions of CRM (Yoshihara and Hamano, 2004), would not satisfy any modern sets of selection criteria (Ueno, 1995), or are only seen as spot reading of the field in a single dyke (Smirnov and Tarduno, 2005) in a dyke swarm showing a weak, but overall stronger field (Halls et al., 2004). Non-Ediacaran weak sustained fields as in the Jurassic (e.g. ~2.8 $*10^{22}$Am^2, Tauxe et al., 2013) or the Devonian (e.g. ~1.1 $*10^{22}$Am^2, Hawkins et al., 2019) are all stronger. However, a field strength behaviour, similar to the one in the Ediacaran, can be observed in the Upper Devonian around ~370 Ma, where site mean palaeointensities as low as 2.4 µT (0.4 $*10^{22}$Am^2) have been reported in the weak time averaged field as well (Hawkins et al., 2019).

The ultra-low Ediacaran intensities are consistent with the predicted weak field state of the geodynamo before the onset of inner core growth (Bono et al., 2019; Driscoll, 2016; Landeau et al., 2017). Under this scenario, the dynamo was operating marginally, powered by thermal convection due to heat loss at the core-mantle boundary alone and the field was diminished. Subsequently, the inner core nucleated providing additional convective power from the release of light elements and latent heat of crystallisation. We cannot, however, rule out an entirely different cause of a massively diminished dipole moment in the Ediacaran, perhaps related to a reconfigured convective pattern in the core perhaps related to an unusual core-mantle heat flow pattern. That the measured palaeointensities are similar in magnitude to ground measurements of the crustal field of Mars, a planet which is suspected to have been without a core dynamo for 4.1 billion years, raises profound questions concerning measurement limits and the history of the geodynamo. Is it even possible to measure geomagnetic-field-derived palaeointensities that are any lower than the values presented here, given the possibility of contamination by a (palaeo-) crustal field? Can we therefore be certain that the geodynamo did not die out altogether in the Ediacaran? Such questions are unfortunately beyond the scope of the present study to answer but motivate urgent future investigations that may yield transformative insights into our planet's history.

5 Conclusions

We report new high quality palaeointensities from eleven sites of the western end of the Grenville dyke swarm. Success rates of palaeointensity experiments were substantially lowered by thermochemical alteration during laboratory heating as well as MD behaviour of the studied rocks. The resulting palaeointensity values range between 1.4 - 7.6 µT (0.33 – 1.76

*10^{22}Am^2). Most of these estimates agree well with results from other palaeointensity studies from this time period (Bono et al., 2019; Shcherbakova et al., 2020) but several palaeointensities are substantially lower with values being similar to values of Mars' crustal field (Johnson et al., 2020). This opens up questions about what geodynamo regimes could result in such weak fields or, to take it one step further, if such weak fields could even suggest an inactive geodynamo. The behaviour of VGPs with almost identical angular dispersion around two clusters argues for the presence of an equatorial dipole field. In contrast, the consistency of presented ultra-low intensities along dykes for both directional components supports the idea of an unstable and/or transitional field in the Ediacaran (Bono et al., 2019; Halls et al., 2015). The presented data are another argument for the Ediacaran field behaving strangely but at this point we are still struggling to define it. However, data for the early to mid-Ediacaran is still scarce and a better coverage of palaeointensity and magnetostratigraphic data would be immensely useful to better characterise the geomagnetic field in the Ediacaran.

Acknowledgements

This study was supported by The Leverhulme Trust (Research Leadership Award, RL-2016-080). We would like to thank R.K. Bono, G. Paterson and S. Lloyd for helpful discussions. Henry Halls would like to thank Alan Lovette for helpful field assistance in finding outcrops of dykes that formed negative topographic features and for many of the paleomagnetic measurements.

Data availability:

Data has been uploaded to a private repository in the MagIC database and will be accessible after publication. Currently, data from this study are available from the corresponding author on reasonable request.

Figures:

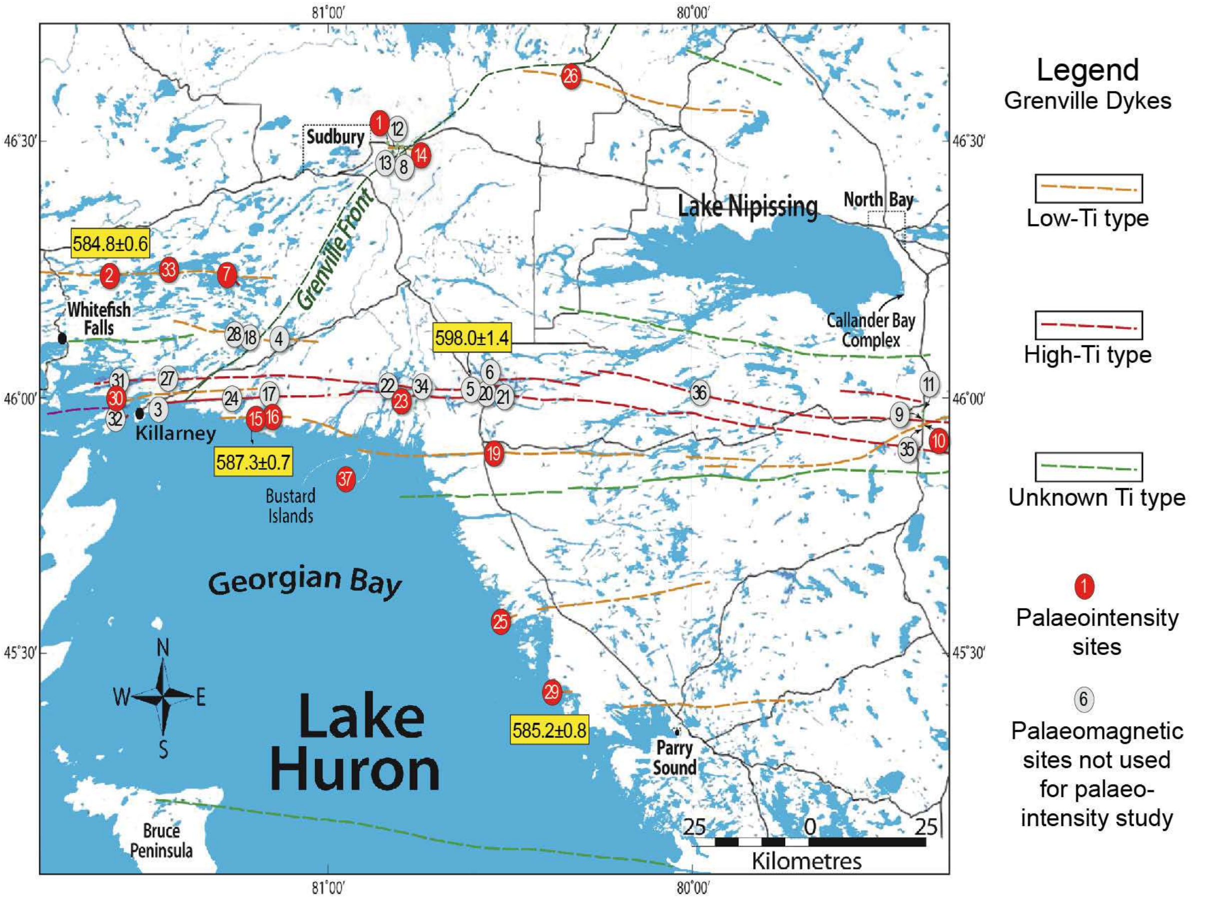

Figure 1: Map of southeast Ontario, showing the Grenville dykes and locations of sites studied in Halls et al. (2015) and sites selected for this palaeointensity study; from Halls et al. (2015)

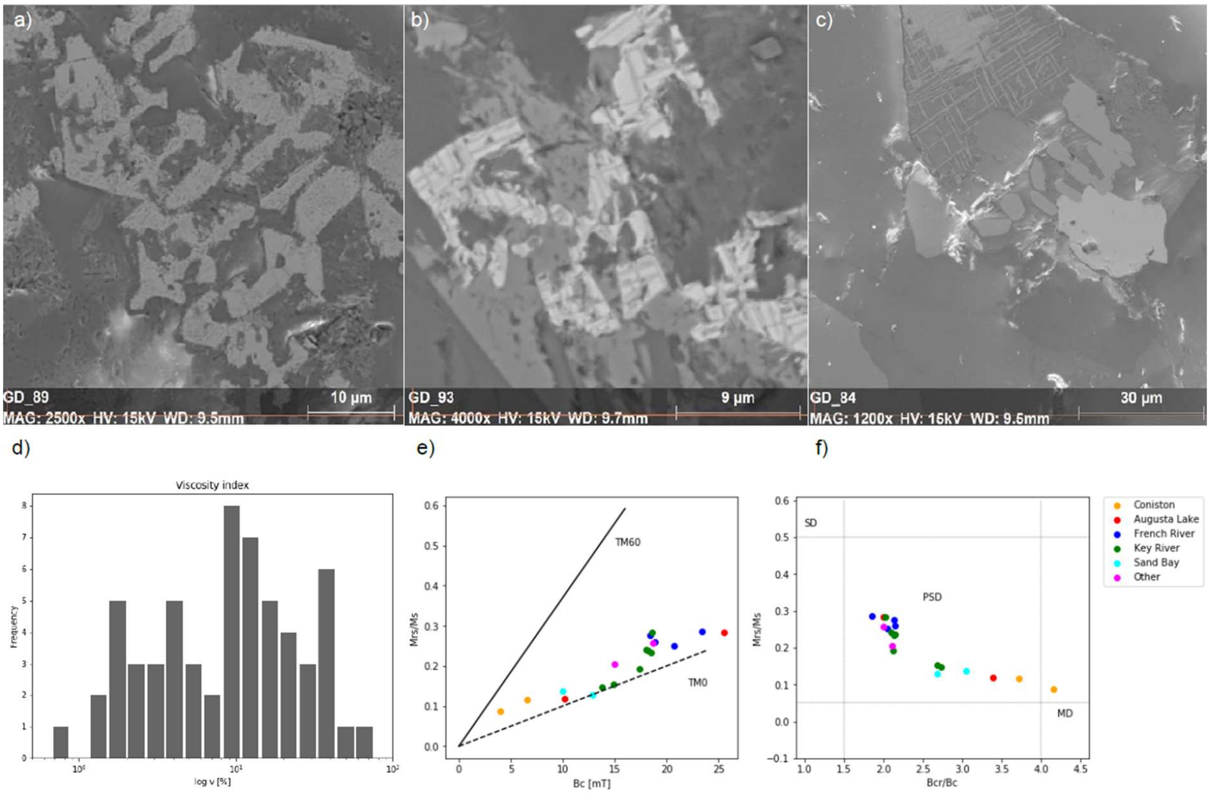

Figure 2: SEM backscatter images: (a) GD23, (b) GD29, examples of dendritic TM grains, (c) GD02, coarse Tm grain, showing magnetite-ilmenite exsolution. (d) frequencies of viscosity indexes of all sites, (e) Hysteresis parameters and (f) Day plot of representative samples of each site.

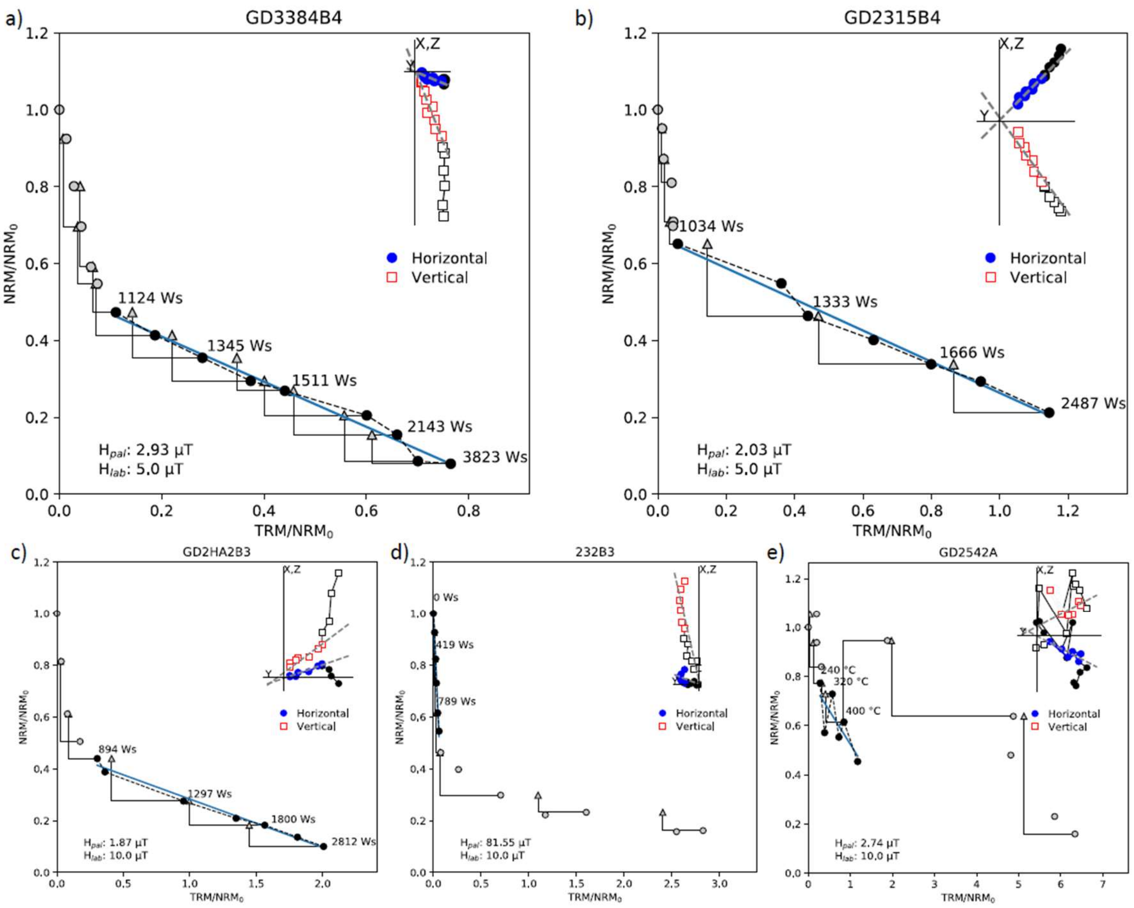

Figure 3: Arai plots of Thellier experiment results. a)-d) show microwave experiments, e) shows a result of a thermal Thellier experiment. For more details, readers are referred to section 3 of the text.

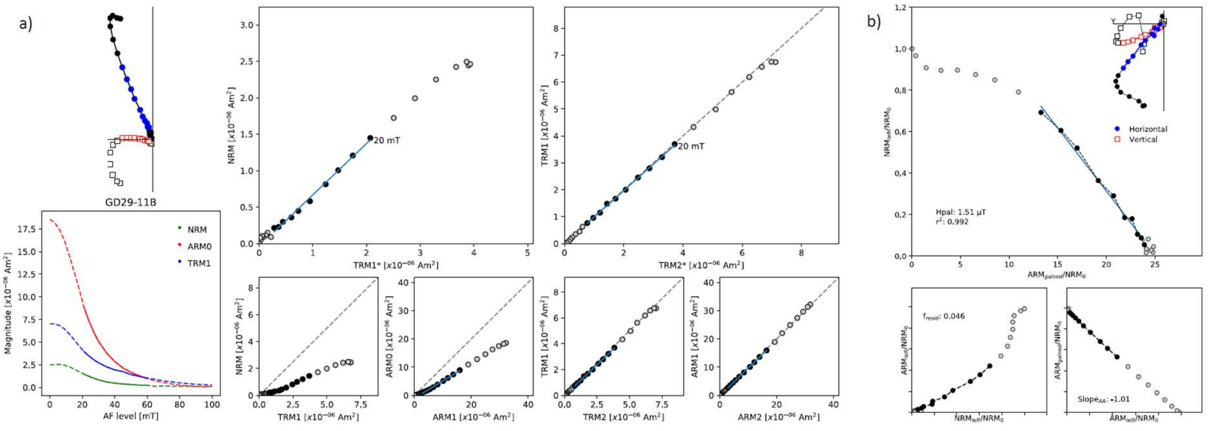

Figure 4: a) Representative example of a successful Shaw experiment: left column shows the orthogonal plot of the demagnetisation of NRM (top) and absolute values of magnetisation

during AF demagnetisations of NRM, ARM0 and TRM1 (bottom). middle and right columns show results from first and second laboratory heating, respectively; b) example of a successful pseudo-Thellier experiment: pseudo-Arai plot with orthogonal projection, demag-demag plot (NRM vs ARM) and ARM-ARM plot (acquisition vs. demagnetisation).

Tables:

		Age [Ma]	Directions (Halls et al 2015)					Intensities [µT]				*pThel [µT]*	VDM [10^{22}Am^2]		
Dyke	Site		N/n	Dec	Inc	a95	k	n/n$_{PI}$	Methods	PI	Std	*PI*	VDM	Std	QPI
Augusta	GD02	584 ±0.6	9/8	120.7	23.1	6.7	69	12/2	MW+S	2.1	0.04	-	0.52	0.01	7
Lake	GD33		8/6	135.6	31.2	8.8	60	17/5	MW	2.6	0.62	*1.9*	0.60	0.14	7
Coniston	GD01		5/3	115.5	17.1	32.4	16	4/0	-	-	-	-	-	-	-
	GD14		13/3	95.5	23.8	26.3	13	6/1	MW	7.6	-	-	1.76	-	6
French River	GD23	598 ±1.4	6/3	132.7	32.6	8.7	202	24/13	MW+S	1.8	0.67	-	0.42	0.15	7
Key	GD10	587 ±0.7	10/9	137.7	75.8	6.7	61	14/0	-	-	-	-	-	-	-
River	GD15		5/5	140.9	66.8	6.7	130	12/1	MW	5.6	-	-	0.88	-	6
	GD16		6/6	163.8	76.7	14.4	22	10/1	MW	4.3	-	*1.3*	0.67	-	6
	GD19		9/5	100.6	56.2	11.9	42	11/0	-	-	-	-	-	-	-
	GD37		8/7	143.1	71.7	5.1	141	6/3	S	5.3	1.57	*3.1*	0.78	0.23	7
Sand Bay	GD29	585 ±0.8	9/9	297	40.1	5.2	97	41/7	MW+S	3.7	0.69	*4.1*	0.80	0.15	8
Other	GD07		7/6	134.8	1.2	11.2	37	1/0	-	-	-	-	-	-	-
Grenville	GD25		9/9	136.5	9.6	8.8	36	14/2	MW+S	6.8	5.82	-	1.74	1.41	7
Dykes	GD26		9/6	130.1	23.8	10.1	45	7/2	S	1.4	0.40	*1.5*	0.33	0.10	6
	GD30		10/6	139	67.3	8.4	64	3/0	-	-	-	-	-	-	-

Table 1: Summary of palaeointensity results of the Grenville dykes: Dyke/Site: dyke/site name, Ages and directional information from Halls et al. (2015), N/n$_{int}$: total number of specimens/ number of successful results, Methods: type of method that contributed successful results (MW: microwave Thellier, TH: thermal Thellier, S: Shaw), PI: palaeointensity results in µT, Std: standard deviation of palaeointensity results (*: standard error of single specimen result instead of multiple specimen

result), pThel: palaeointensity results in µT from pseudo-Thellier experiments. Values are shown as comparison to the results from the heating methods but are not used in the calculation of the mean palaeointensities. VDM: virtual dipole moment in $10^{22}Am^2$, Std: standard deviation of VDM results, QPI values of sites.

References:

Abrajevitch, A., Van der Voo Rob, R., 2010. Incompatible Ediacaran paleomagnetic directions suggest an equatorial geomagnetic dipole hypothesis. Earth Planet. Sci. Lett. https://doi.org/10.1016/j.epsl.2010.02.038

Aubert, J., Wicht, J., 2004. Axial vs. equatorial dipolar dynamo models with implications for planetary magnetic fields. Earth Planet. Sci. Lett. https://doi.org/10.1016/S0012-821X(04)00102-5

Bazhenov, M.L., Levashova, N.M., Meert, J.G., Golovanova, I. V., Danukalov, K.N., Fedorova, N.M., 2016. Late Ediacaran magnetostratigraphy of Baltica: Evidence for Magnetic Field Hyperactivity? Earth Planet. Sci. Lett. https://doi.org/10.1016/j.epsl.2015.12.015

Biggin, A.J., Paterson, G.A., 2014. A new set of qualitative reliability criteria to aid inferences on palaeomagnetic dipole moment variations through geological time. Front. Earth Sci. https://doi.org/10.3389/feart.2014.00024

Biggin, A.J., Perrin, M., Dekkers, M.J., 2007. A reliable absolute palaeointensity determination obtained from a non-ideal recorder. Earth Planet. Sci. Lett. https://doi.org/10.1016/j.epsl.2007.03.017

Biggin, A.J., Piispa, E.J., Pesonen, L.J., Holme, R., Paterson, G.A., Veikkolainen, T., Tauxe, L.,

2015. Palaeomagnetic field intensity variations suggest Mesoproterozoic inner-core nucleation. Nature. https://doi.org/10.1038/nature15523

Bono, R.K., Tarduno, J.A., 2014. A stable ediacaran earth recorded by single silicate crystals of the ca. 565 Ma sept-Îles intrusion. Geology. https://doi.org/10.1130/G36247.1

Bono, R.K., Tarduno, J.A., Nimmo, F., Cottrell, R.D., 2019. Young inner core inferred from Ediacaran ultra-low geomagnetic field intensity. Nat. Geosci. https://doi.org/10.1038/s41561-018-0288-0

Brown, M.C., Gratton, M.N., Shaw, J., Holme, R., Soler, V., 2009. Microwave palaeointensity results from the Matuyama-Brunhes geomagnetic field reversal. Phys. Earth Planet. Inter. https://doi.org/10.1016/j.pepi.2008.11.001

Day, R., Fuller, M., Schmidt, V.A., 1977. Hysteresis properties of titanomagnetites: Grain-size and compositional dependence. Phys. Earth Planet. Inter. https://doi.org/10.1016/0031-9201(77)90108-X

Doubrovine, P. V., Veikkolainen, T., Pesonen, L.J., Piispa, E., Ots, S., Smirnov, A. V., Kulakov, E. V., Biggin, A.J., 2019. Latitude Dependence of Geomagnetic Paleosecular Variation and its Relation to the Frequency of Magnetic Reversals: Observations From the Cretaceous and Jurassic. Geochemistry, Geophys. Geosystems. https://doi.org/10.1029/2018GC007863

Driscoll, P.E., 2016. Simulating 2 Ga of geodynamo history. Geophys. Res. Lett. https://doi.org/10.1002/2016GL068858

Evans, D.A.D., Raub, T.D., 2011. Chapter 7: Neoproterozoic glacial palaeolatitudes: A global update. Geol. Soc. Mem. https://doi.org/10.1144/M36.7

Gissinger, C., Petitdemange, L., Schrinner, M., Dormy, E., 2012. Bistability between equatorial and axial dipoles during magnetic field reversals. Phys. Rev. Lett. https://doi.org/10.1103/PhysRevLett.108.234501

Halls, H.C., Lovette, A., Hamilton, M., Söderlund, U., 2015. A paleomagnetic and U-Pb geochronology study of the western end of the Grenville dyke swarm: Rapid changes in paleomagnetic field direction at ca. 585Ma related to polarity reversals? Precambrian Res. https://doi.org/10.1016/j.precamres.2014.11.029

Halls, H.C., McArdle, N.J., Gratton, M.N., Hill, M.J., Shaw, J., 2004. Microwave paleointensities from dyke chilled margins: A way to obtain long-term variations in geodynamo intensity for the last three billion years. Phys. Earth Planet. Inter. https://doi.org/10.1016/j.pepi.2004.03.013

Hawkins, L.M.A., Anwar, T., Shcherbakova, V. V., Biggin, A.J., Kravchinsky, V.A., Shatsillo, A. V., Pavlov, V.E., 2019. An exceptionally weak Devonian geomagnetic field recorded by the Viluy Traps, Siberia. Earth Planet. Sci. Lett. https://doi.org/10.1016/j.epsl.2018.10.035

Hill, M.J., Shaw, J., 1999. Palaeointensity results for historic lavas from Mt Etna using microwave demagnetization/remagnetization in a modified Thellier-type experiment. Geophys. J. Int. https://doi.org/10.1046/j.1365-246X.1999.00980.x

Hyodo, H., Dunlop, D.J., 1993. Effect of anisotropy on the paleomagnetic contact test for a Grenville Dike. J. Geophys. Res. https://doi.org/10.1029/92JB02915

Johnson, C.L., Mittelholz, A., Langlais, B., Russell, C.T., Ansan, V., Banfield, D., Chi, P.J., Fillingim, M.O., Forget, F., Haviland, H.F., Golombek, M., Joy, S., Lognonné, P., Liu, X., Michaut, C., Pan, L., Quantin-Nataf, C., Spiga, A., Stanley, S., Thorne, S.N., Wieczorek, M.A., Yu, Y., Smrekar, S.E., Banerdt, W.B., 2020. Crustal and time-varying magnetic fields at the InSight landing site on Mars. Nat. Geosci. https://doi.org/10.1038/s41561-020-0537-x

Kirschvink, J.L., Ripperdan, R.L., Evans, D.A., 1997. Evidence for a large-scale reorganization of Early Cambrian continental masses by inertial interchange true polar wander. Science (80-.). https://doi.org/10.1126/science.277.5325.541

Kissel, C., Laj, C., 2004. Improvements in procedure and paleointensity selection criteria (PICRIT-03) for Thellier and Thellier determinations: Application to Hawaiian basaltic long cores. Phys. Earth Planet. Inter. https://doi.org/10.1016/j.pepi.2004.06.010

Kodama, K.P., Carnes, L.K., Tarduno, J.A., Berti, C., 2019. Palaeointensity of the 1.3 billion-yr-old Gardar basalts, southern Greenland revisited: No evidence for onset of inner core growth. Geophys. J. Int. https://doi.org/10.1093/gji/ggz126

Kulakov, E. V., Sprain, C.J., Doubrovine, P. V., Smirnov, A. V., Paterson, G.A., Hawkins, L., Fairchild, L., Piispa, E.J., Biggin, A.J., 2019. Analysis of an Updated Paleointensity Database (QPI-PINT) for 65–200 Ma: Implications for the Long-Term History of Dipole Moment Through the Mesozoic. J. Geophys. Res. Solid Earth. https://doi.org/10.1029/2018JB017287

Landeau, M., Aubert, J., Olson, P., 2017. The signature of inner-core nucleation on the geodynamo. Earth Planet. Sci. Lett. https://doi.org/10.1016/j.epsl.2017.02.004

Lawley, E.A., 1970. The intensity of the geomagnetic field in Iceland during neogene polarity transitions and systematic deviations. Earth Planet. Sci. Lett.

https://doi.org/10.1016/0012-821X(70)90076-2

Leonhardt, R., Soffel, H.C., 2002. A reversal of the Earth's magnetic field recorded in mid-Miocene lava flows of Gran Canaria: Paleointensities. J. Geophys. Res. Solid Earth. https://doi.org/10.1029/2001jb000949

Li, Z.X., Evans, D.A.D., Halverson, G.P., 2013. Neoproterozoic glaciations in a revised global palaeogeography from the breakup of Rodinia to the assembly of Gondwanaland. Sediment. Geol. https://doi.org/10.1016/j.sedgeo.2013.05.016

McCausland, P.J.A., Hodych, J.P., 1998. Paleomagnetism of the 550 Ma Skinner Cove volcanics of western Newfoundland and the opening of the Iapetus Ocean. Earth Planet. Sci. Lett. https://doi.org/10.1016/S0012-821X(98)00171-X

McCausland, P.J.A., Van der Voo, R., Hall, C.M., 2007. Circum-Iapetus paleogeography of the Precambrian-Cambrian transition with a new paleomagnetic constraint from Laurentia. Precambrian Res. https://doi.org/10.1016/j.precamres.2007.03.004

Meert, J.G., 2014. Ediacaran-Early Ordovician paleomagnetism of Baltica: A review. Gondwana Res. https://doi.org/10.1016/j.gr.2013.02.003

Meert, J.G., Van Der Voo, R., Payne, T.W., 1994. Paleomagnetism of the Catoctin volcanic province: a new Vendian- Cambrian apparent polar wander path for North America. J. Geophys. Res. https://doi.org/10.1029/93JB01723

Murthy, G.S., 1971. The Paleomagnetism of Diabase Dikes from the Grenville Province. Can. J. Earth Sci. https://doi.org/10.1139/e71-075

Paterson, G.A., 2011. A simple test for the presence of multidomain behavior during paleointensity experiments. J. Geophys. Res. Solid Earth.

https://doi.org/10.1029/2011JB008369

Paterson, G.A., Heslop, D., Muxworthy, A.R., 2010. Deriving confidence in paleointensity estimates. Geochemistry, Geophys. Geosystems. https://doi.org/10.1029/2010GC003071

Paterson, G.A., Heslop, D., Pan, Y., 2016. The pseudo-Thellier palaeointensity method: New calibration and uncertainty estimates. Geophys. J. Int. https://doi.org/10.1093/gji/ggw349

Paterson, G.A., Tauxe, L., Biggin, A.J., Shaar, R., Jonestrask, L.C., 2014. On improving the selection of Thellier-type paleointensity data. Geochemistry, Geophys. Geosystems. https://doi.org/10.1002/2013GC005135

Prévot, M., 1981. Some aspects of magnetic viscosity in subaerial and submarine volcanic rocks. Geophys. J. R. Astron. Soc. https://doi.org/10.1111/j.1365-246X.1981.tb05952.x

Riisager, P., Riisager, J., 2001. Detecting multidomain magnetic grains in Thellier palaeointensity experiments. Phys. Earth Planet. Inter. https://doi.org/10.1016/S0031-9201(01)00236-9

Robert, B., Besse, J., Blein, O., Greff-Lefftz, M., Baudin, T., Lopes, F., Meslouh, S., Belbadaoui, M., 2017. Constraints on the Ediacaran inertial interchange true polar wander hypothesis: A new paleomagnetic study in Morocco (West African Craton). Precambrian Res. https://doi.org/10.1016/j.precamres.2017.04.010

Rolph, T.C., Shaw, J., 1985. A new method of palaeofield magnitude correction for thermally altered samples and its application to Lower Carboniferous lavas. Geophys. J. R. Astron. Soc. https://doi.org/10.1111/j.1365-246X.1985.tb05124.x

Shaar, R., Tauxe, L., 2015. Instability of thermoremanence and the problem of estimating the ancient geomagnetic field strength from non-single-domain recorders. Proc. Natl. Acad. Sci. U. S. A. https://doi.org/10.1073/pnas.1507986112

Shcherbakov, V.P., Gribov, S.K., Lhuillier, F., Aphinogenova, N.A., Tsel’movich, V.A., 2019. On the Reliability of Absolute Palaeointensity Determinations on Vasaltic Rocks Bearing a Thermochemical Remanence. J. Geophys. Res. Solid Earth. https://doi.org/10.1029/2019JB017873

Shcherbakova, V. V., Bakhmutov, V.G., Thallner, D., Shcherbakov, V.P., Zhidkov, G. V., Biggin, A.J., 2020. Ultra-low palaeointensities from East European Craton, Ukraine support a globally anomalous palaeomagnetic field in the Ediacaran. Geophys. J. Int. 220, 1928–1946. https://doi.org/10.1093/gji/ggz566

Shcherbakova, V. V., Biggin, A.J., Veselovskiy, R. V., Shatsillo, A. V., Hawkins, L.M.A., Shcherbakov, V.P., Zhidkov, G. V., 2017. Was the Devonian geomagnetic field dipolar or multipolar? Palaeointensity studies of Devonian igneous rocks from the Minusa Basin (Siberia) and the Kola Peninsula dykes, Russia. Geophys. J. Int. https://doi.org/10.1093/gji/ggx085

Smirnov, A. V., Kulakov, E. V., Foucher, M.S., Bristol, K.E., 2017. Intrinsic paleointensity bias and the long-term history of the geodynamo. Sci. Adv. https://doi.org/10.1126/sciadv.1602306

Smirnov, A. V., Tarduno, J.A., 2005. Thermochemical remanent magnetization in Precambrian rocks: Are we sure the geomagnetic field was weak? J. Geophys. Res. Solid Earth. https://doi.org/10.1029/2004JB003445

Tanczyk, E.I., Lapointe, P., Morris, W.A., Schmidt, P.W., 1987. A paleomagnetic study of the layered mafic intrusion at Sept- Iles, Quebec (Canada). Can. J. Earth Sci. https://doi.org/10.1139/e87-135

Tauxe, L., Gee, J.S., Steiner, M.B., Staudigel, H., 2013. Paleointensity results from the Jurassic: New constraints from submarine basaltic glasses of ODP Site 801C. Geochemistry, Geophys. Geosystems. https://doi.org/10.1002/ggge.20282

Tauxe, L., Pick, T., Kok, Y.S., 1995. Relative paleointensity in sediments: A Pseudo-Thellier Approach. Geophys. Res. Lett. https://doi.org/10.1029/95GL03166

Tauxe, L., Staudigel, H., 2004. Strength of the geomagnetic field in the cretaceous normal superchron: New data from submarine basaltic glass of the troodos ophiolite. Geochemistry, Geophys. Geosystems. https://doi.org/10.1029/2003GC000635

Tsunakawa, H., Shaw, J., 1994. The Shaw method of palaeointensity determinations and its application to recent volcanic rocks. Geophys. J. Int. https://doi.org/10.1111/j.1365-246X.1994.tb03999.x

Ueno, H., Irving, E., McNutt, R.H., 1975. Paleomagnetism of the Whitestone Anorthosite and Diorite, the Grenville Polar Track, and Relative Motions of the Laurentian and Baltic Shields. Can. J. Earth Sci. https://doi.org/10.1139/e75-019

Ueno, N., 1995. Geomagnetic palaeointensity experiment on igneous and metamorphic rocks from Enderby land in Napier Complex, Antarctica. Proc. NIPR Symp. Antarct. Geosci. 8, 193–200.

Veikkolainen, T., Pesonen, L.J., 2014. Palaeosecular variation, field reversals and the stability of the geodynamo in the Precambrian. Geophys. J. Int.

https://doi.org/10.1093/gji/ggu348

Wang, D., Van der Voo, R., 2004. The hysteresis properties of multidomain magnetite and titanomagnetite/titanomaghemite in mid-ocean ridge basalts. Earth Planet. Sci. Lett. https://doi.org/10.1016/S0012-821X(04)00052-4

Yamamoto, Y., Shibuya, H., Tanaka, H., Hoshizumi, H., 2010. Geomagnetic paleointensity deduced for the last 300kyr from Unzen Volcano, Japan, and the dipolar nature of the Iceland Basin excursion. Earth Planet. Sci. Lett. https://doi.org/10.1016/j.epsl.2010.02.024

Yoshihara, A., Hamano, Y., 2004. Paleomagnetic constraints on the Archean geomagnetic field intensity obtained from komatiites of the Barberton and Belingwe greenstone belts, South Africa and Zimbabwe. Precambrian Res. https://doi.org/10.1016/j.precamres.2004.01.003

Yu, Y., Tauxe, L., 2005. Testing the IZZI protocol of geomagnetic field intensity determination. Geochemistry, Geophys. Geosystems. https://doi.org/10.1029/2004GC000840

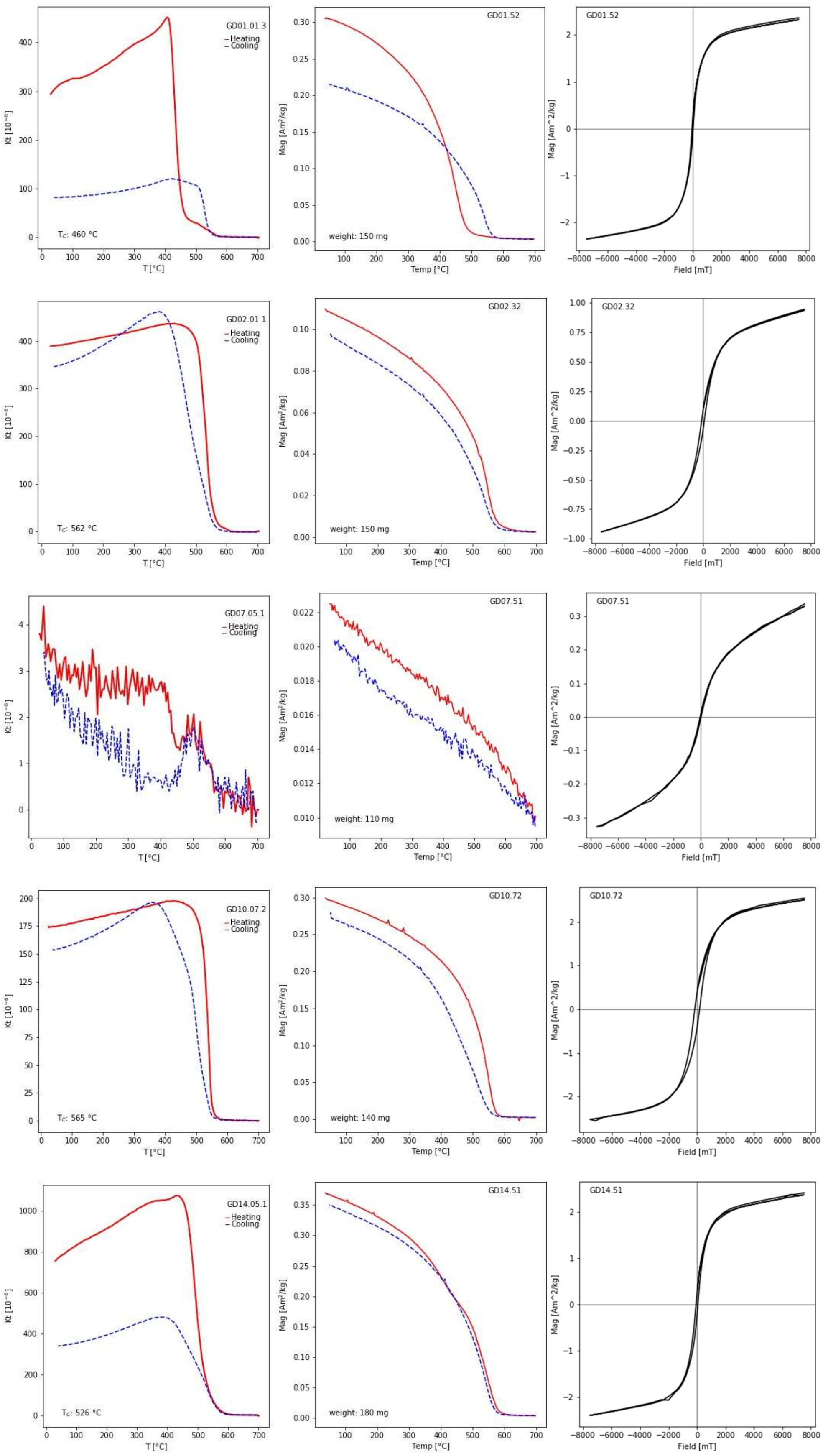
GD01.01.3
Heating
Cooling
T_C: 460 °C
Kt [10^-6]
T [°C]
GD01.52
weight: 150 mg
Mag [Am²/kg]
Temp [°C]
GD01.52
Mag [Am^2/kg]
Field [mT]
GD02.01.1
Heating
Cooling
T_C: 562 °C
Kt [10^-6]
T [°C]
GD02.32
weight: 150 mg
Mag [Am²/kg]
Temp [°C]
GD02.32
Mag [Am^2/kg]
Field [mT]
GD07.05.1
Heating
Cooling
Kt [10^-6]
T [°C]
GD07.51
weight: 110 mg
Mag [Am²/kg]
Temp [°C]
GD07.51
Mag [Am^2/kg]
Field [mT]
GD10.07.2
Heating
Cooling
T_C: 565 °C
Kt [10^-6]
T [°C]
GD10.72
weight: 140 mg
Mag [Am²/kg]
Temp [°C]
GD10.72
Mag [Am^2/kg]
Field [mT]
GD14.05.1
Heating
Cooling
T_C: 526 °C
Kt [10^-6]
T [°C]
GD14.51
weight: 180 mg
Mag [Am²/kg]
Temp [°C]
GD14.51
Mag [Am^2/kg]
Field [mT]

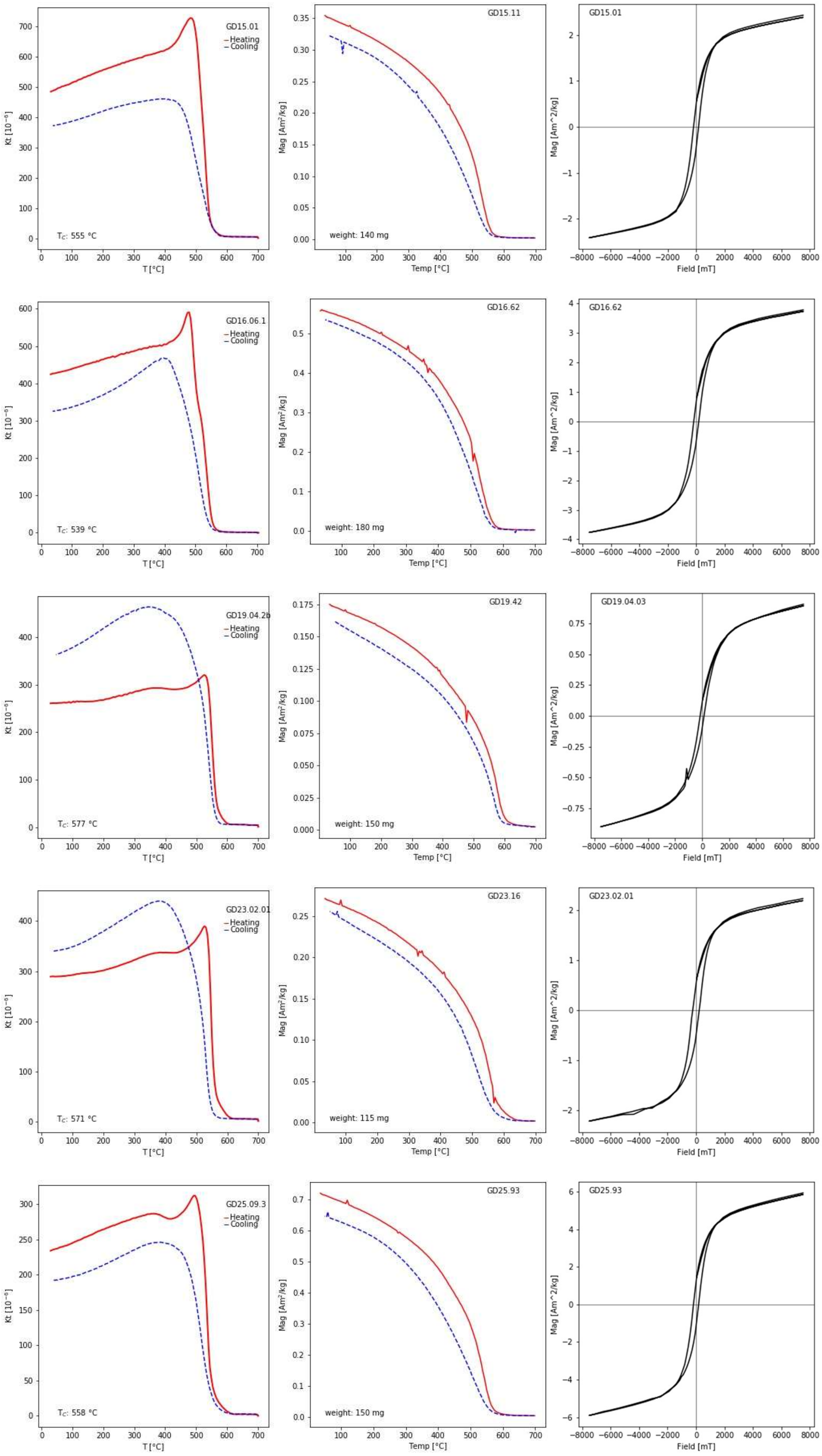
GD15.01
Heading
Cooling
Kt [10⁻⁶]
T [°C]
T_C: 555 °C
GD15.11
Mag [Am²/kg]
Temp [°C]
weight: 140 mg
GD15.01
Mag [Am^2/kg]
Field [mT]
GD16.06.1
Heating
Cooling
Kt [10⁻⁶]
T [°C]
T_C: 539 °C
GD16.62
Mag [Am²/kg]
Temp [°C]
weight: 180 mg
GD16.62
Mag [Am^2/kg]
Field [mT]
GD19.04.2b
Heating
Cooling
Kt [10⁻⁶]
T [°C]
T_C: 577 °C
GD19.42
Mag [Am²/kg]
Temp [°C]
weight: 150 mg
GD19.04.03
Mag [Am^2/kg]
Field [mT]
GD23.02.01
Heating
Cooling
Kt [10⁻⁶]
T [°C]
T_C: 571 °C
GD23.16
Mag [Am²/kg]
Temp [°C]
weight: 115 mg
GD23.02.01
Mag [Am^2/kg]
Field [mT]
GD25.09.3
Heating
Cooling
Kt [10⁻⁶]
T [°C]
T_C: 558 °C
GD25.93
Mag [Am²/kg]
Temp [°C]
weight: 150 mg
GD25.93
Mag [Am^2/kg]
Field [mT]
0
100
200
300
400
500
600
700
−8000
−6000
−4000
−2000
0
2000
4000
6000
8000

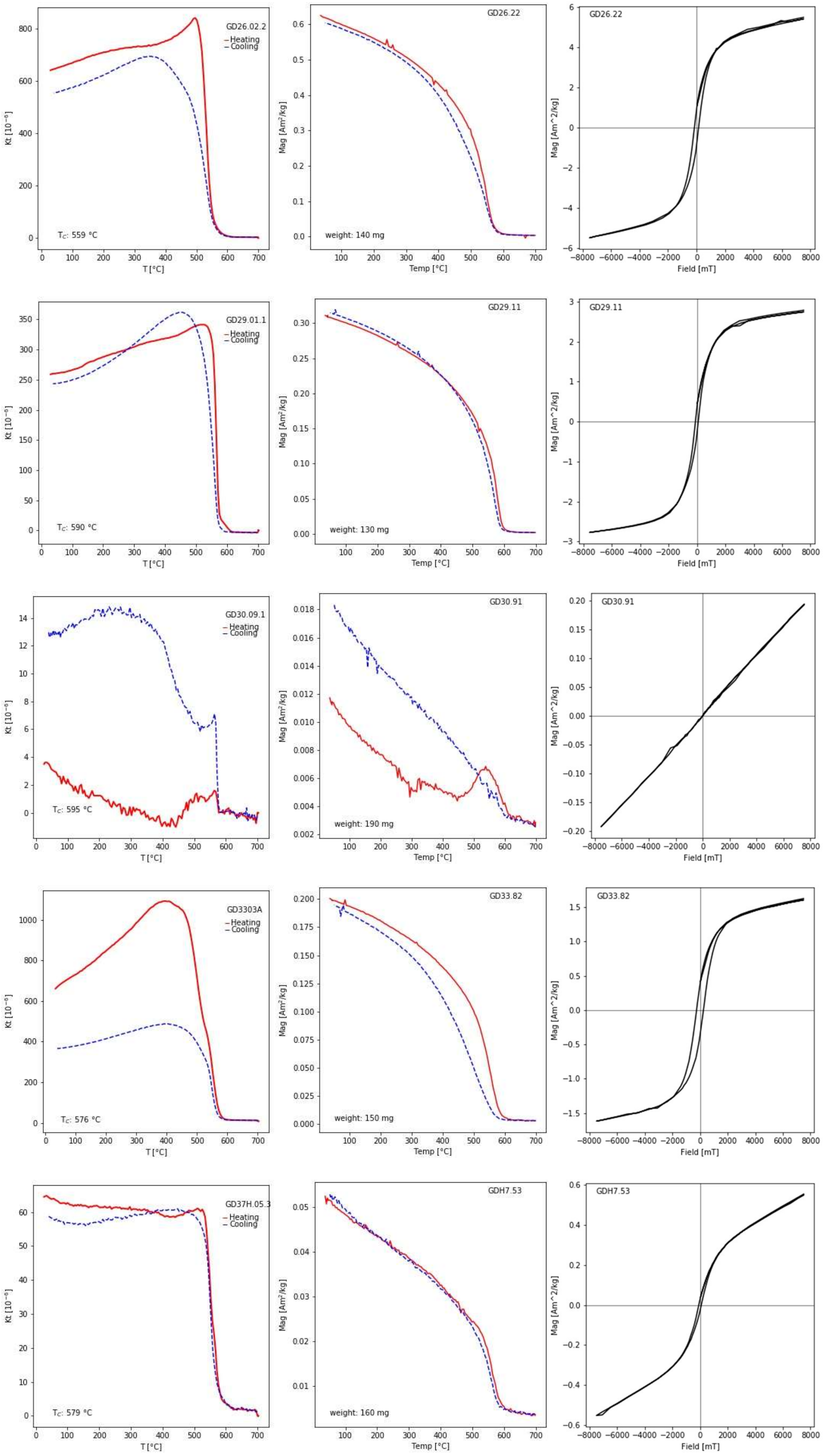

Supplementary Figure 1: Representative rock magnetic measurement plots for each site: left: susceptibility vs temperature plots; centre: thermomagnetic curves; right: hysteresis plots a)

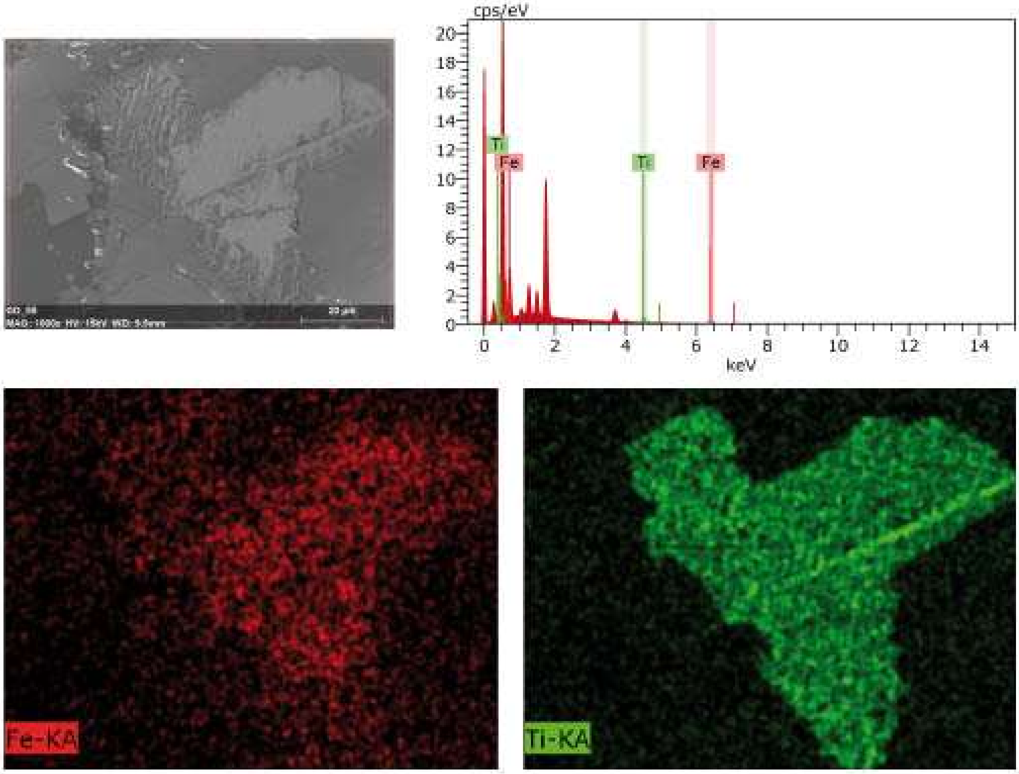
20 µm
cps/eV
20
18
16
14
12
10
8
6
4
2
0
Ti
Fe
Ti
Fe
0
2
4
6
8
10
12
14
keV
Fe-KA
Ti-KA

b)

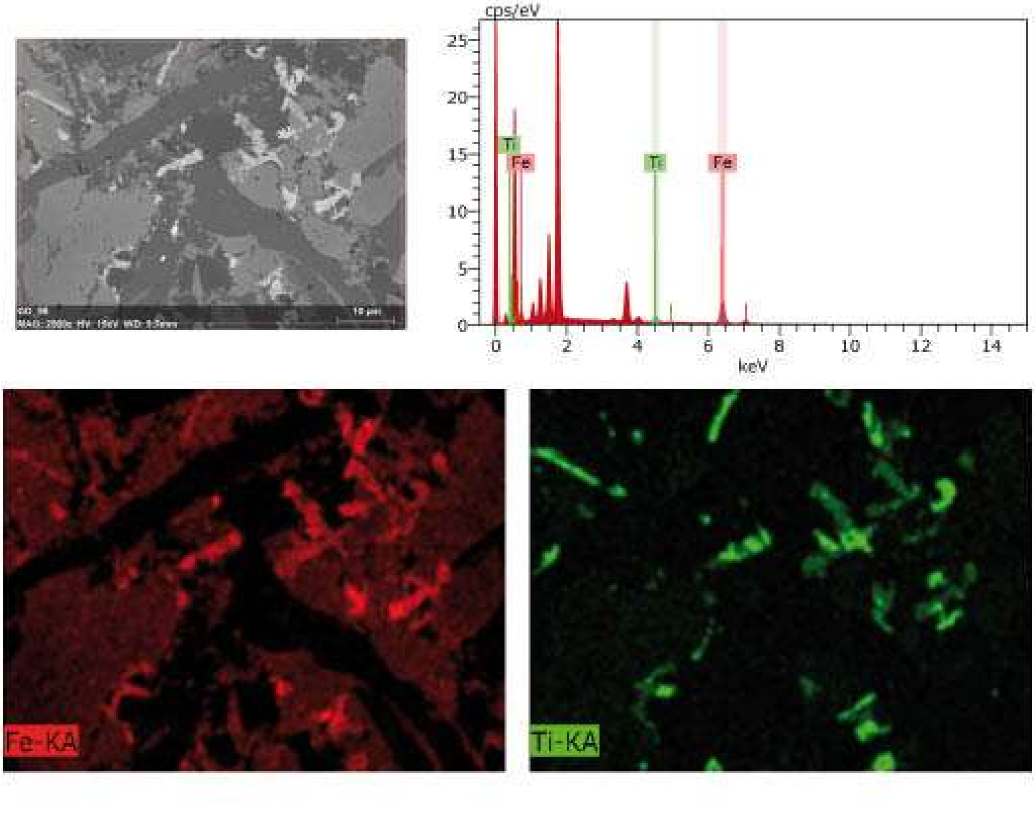
10 µm
cps/eV
25
20
15
10
5
0
Ti
Fe
Ti
Fe
0
2
4
6
8
10
12
14
keV
Fe-KA
Ti-KA

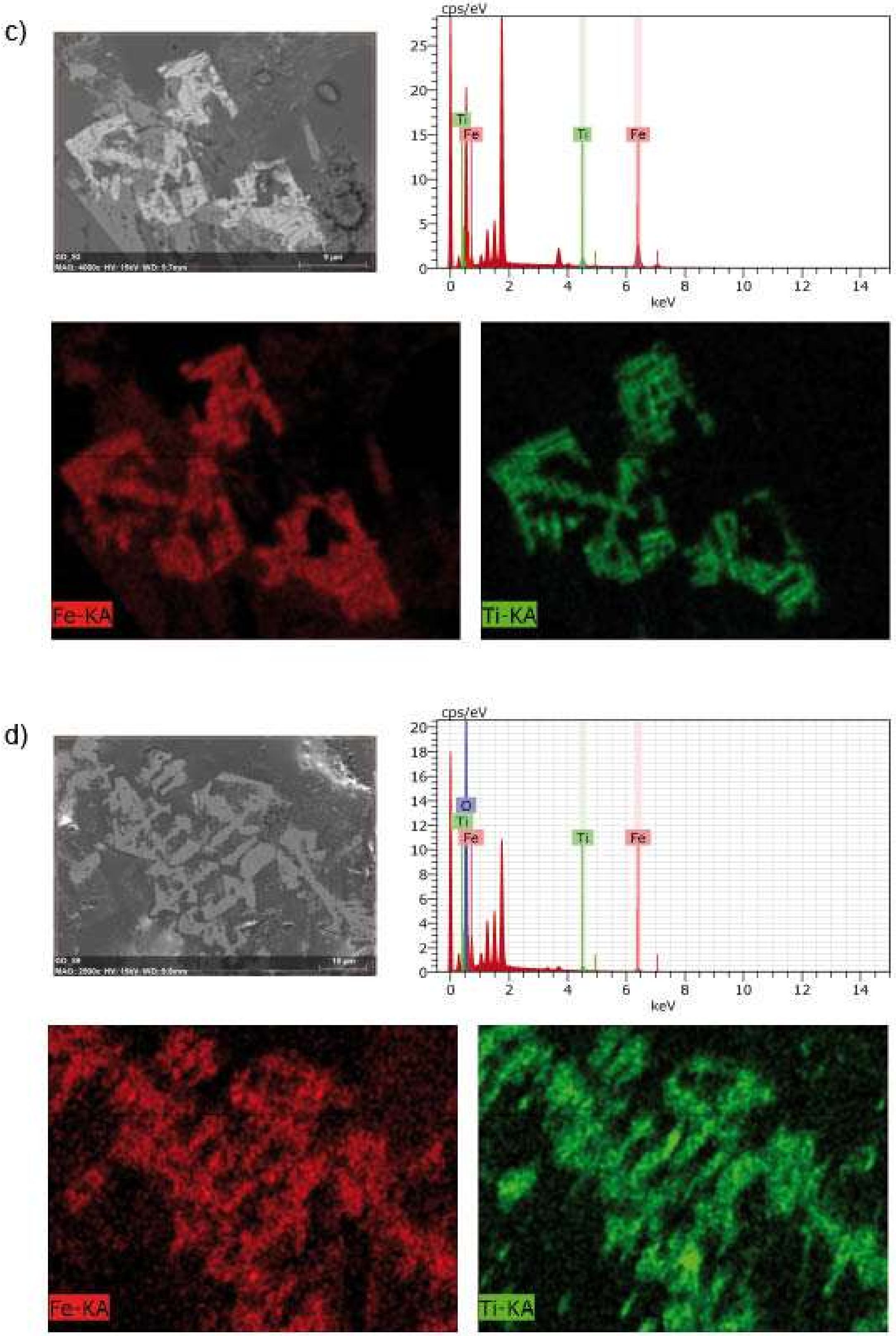

Supplementary Figure 2: Elemental composition maps for Fe and Ti from BSE analysis: a) Site GD02 host rock at Augusta Lake dyke; b) Site GD33 Augusta Lake Dyke; c) GD29, Sand Bay Dyke, d) Site GD23; French River Dyke

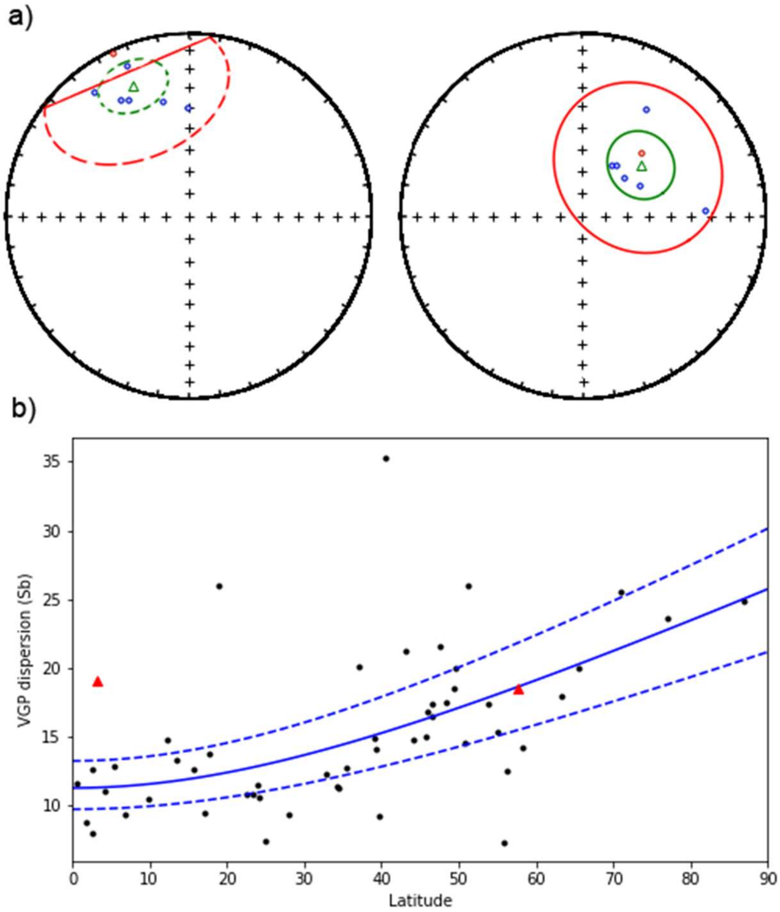

Supplementary figure 3: Palaeosecular variation. (a) Filtered VGPs (nn ≥ 5, k ≥ 30) of shallow (right) and steep (left) directional component from Halls et al., (2015). Open circles indicate negative inclination. Red markers show VGPs with flipped polarity. Green triangles and circles show mean VGP and 95% confidence intervals. Variable cutoff values (Vandamme, 1994) are plotted as red circles. (b) angular dispersion of the Grenville dyke components (green triangles) compared to dispersion values from PSV10 and model G fit (blue line) with 95% bootstrap uncertainty interval (dashed lines) (Cromwell et al., 2018).

References:

Biggin, A.J., Paterson, G.A., 2014. A new set of qualitative reliability criteria to aid inferences on palaeomagnetic dipole moment variations through geological time. Front. Earth Sci. https://doi.org/10.3389/feart.2014.00024

Biggin, A.J., Perrin, M., Dekkers, M.J., 2007. A reliable absolute palaeointensity determination obtained from a non-ideal recorder. Earth Planet. Sci. Lett. https://doi.org/10.1016/j.epsl.2007.03.017

Cromwell, G., Johnson, C.L., Tauxe, L., Constable, C.G., Jarboe, N.A., 2018. PSV10: A Global Data Set for 0–10 Ma Time-Averaged Field and Paleosecular Variation Studies. Geochemistry, Geophys. Geosystems. https://doi.org/10.1002/2017GC007318

Halls, H.C., Lovette, A., Hamilton, M., Söderlund, U., 2015. A paleomagnetic and U-Pb geochronology study of the western end of the Grenville dyke swarm: Rapid changes in paleomagnetic field direction at ca. 585Ma related to polarity reversals? Precambrian Res. https://doi.org/10.1016/j.precamres.2014.11.029

Kissel, C., Laj, C., 2004. Improvements in procedure and paleointensity selection criteria (PICRIT-03) for Thellier and Thellier determinations: Application to Hawaiian basaltic long cores. Phys. Earth Planet. Inter. https://doi.org/10.1016/j.pepi.2004.06.010

Leonhardt, R., Krása, D., Coe, R.S., 2004. Multidomain behavior during Thellier paleointensity experiments: A phenomenological model. Phys. Earth Planet. Inter. https://doi.org/10.1016/j.pepi.2004.01.009

Paterson, G.A., Biggin, A.J., Hodgson, E., Hill, M.J., 2015. Thellier-type paleointensity data from multidomain specimens. Phys. Earth Planet. Inter. https://doi.org/10.1016/j.pepi.2015.06.003

Vandamme, D., 1994. A new method to determine paleosecular variation. Phys. Earth Planet. Inter. https://doi.org/10.1016/0031-9201(94)90012-4

Specimen	B anc	H lab	I/Tmin	I/Tmax	n	FRAC	β	q	k'	MADa	α	DRAT	CDRAT	DRATTail	Method
GD0232B2	3	10	107.35	237.28	5	0.367	0.140	3.6	0.459	2.9	4.1	1.9	2.6		MW IZZI
GD0232B3	2.2	10	128.88	227	4	0.234	0.097	3.4	0.391	4.6	7.4	1.2	3.6		MW IZZI
GD0232B4	3.3	10	104.38	195.81	4	0.267	0.173	1.5	1.046	1.7	1.5	31.7	29.3		MW IZZI
GD0232B5	1.9	3	167.09	427.37	6	0.241	0.056	8.3	0.291	4.7	11.7	20	7.8		MW IZZI
GD02HA2B2	2.5	10	44.39	151.19	6	0.397	0.094	4.4	-0.067	6.2	19.5	14.6	18.5		MW IZZI
GD02HA2B3	2.1	10	67.03	277.14	8	0.431	0.068	9.4	0.438	7	7.8	6	2.1		MW IZZI
GD02HA2B4	9.6	15	43.86	106.88	4	0.206	0.155	2.8	0.571	4.1	5	0.7	0.4		MW IZZI
GD02HA2B5	6.2	15	44.32	102.99	4	0.249	0.141	2.2	0.579	2.8	5.4	4.3	4.8		MW IZZI
GD02HA2B6	4	5	44.91	150	6	0.291	0.084	4.9	0.505	5.8	12.4	13.3	18.9		MW IZZI
GD3301B1	7.6	10	84.88	136.05	4	0.212	0.342	0.6	-1.819	8.3	20.2	17.7	15.1		MW IZZI
GD3301B2	3.8	10	132.12	287.55	4	0.287	0.242	2.0	0.88	5.1	3.4	53.5	73.4		MW IZZI
GD3301B3	2.8	5	136.13	255.78	5	0.185	0.097	5.2	0.237	11.1	2.7	33.2	13		MW IZZI
GD3301B4	7.7	5	62.38	118.12	4	0.307	0.134	2.0	0.622	2.5	5.2	5.1	3.2		MW IZZI
GD3301B5	5.7	15	43.75	97.25	4	0.233	0.154	2.3	0.638	6.1	9.9	9.8	10.8		MW IZZI
GD3301B6	10.5	15	43.78	122.69	6	0.412	0.097	5.7	0.489	7.4	10.2	12	2.4		MW IZZI
GD3382B2	2.7	5	138	651.9	7	0.317	0.091	4.8	-0.424	7.6	21.9	9.7	13.5		MW IZZI
GD3382B3	3.1	5	111.98	293.03	6	0.412	0.082	7.4	0.234	4.2	1.6	9.4	2.3		MW IZZI
GD3382B4	2.9	5	89.15	186.16	5	0.286	0.122	3.6	0.413	6.8	10.5	12.7	18.3		MW IZZI
GD3384B1	1.7	5	102.94	372.33	9	0.364	0.084	6.2	0.444	3.3	8.5	6.4	2.6		MW IZZI
GD3384B2	2	5	100.09	404.37	10	0.380	0.067	8.2	0.25	3.8	11.2	6.3	13.6		MW IZZI
GD3384B3	3.2	10	114.69	280.13	8	0.398	0.078	8.0	0.203	5.7	6	9.1	12.7		MW IZZI
GD3384B4	3	5	112.66	387.87	9	0.418	0.047	13.5	-0.031	3.4	3	6.9	9.1	5.1	MW IZZI
GD3384B5	1.9	5	112.36	269.95	8	0.255	0.136	2.5	0.255	3.7	15.9	24.1	14.7		MW IZZI
GD0232A	11.6	10	0	150	3	0.006	0.428	0.1	0.152	1.1	24.6	33.1	33.1		TH IZZI
GD3301	2.5	10	460	550	4	0.051	0.030	7.9	-0.006	20.5	28.5	95	129.2		TH IZZI
GD0152B1	2	5	113.39	210.83	4	0.404	0.362	0.8	-1.391	23.8	17.6	66.7	72.7		MW IZZI
GD0152B2	1.8	5	83.66	213.31	5	0.392	0.300	1.6	-1.015	14.8	27.1	52.8	57.5		MW IZZI
GD0161B1	41.3	10	0	119.31	7	0.418	0.144	1.4	-0.721	12.6	41.8	6.1	2.7		MW IZZI
GD1451B1	7.6	5	64.22	200.86	7	0.414	0.090	4.7	0.27	4	9.6	12.8	9.2		MW IZZI
GD1451B2	6	5	84.12	134.89	3	0.236	0.066	2.0	0.242	8.1	22.6	6.7	7.2		MW IZZI
GD0161A	25.1	10	0	150	3	0.004	0.349	0.0	1.519	1.9	29.6	0.7	0.7		TH IZZI
GD1462B	1.9	10	320	490	6	0.368	0.258	0.4	0.749	25.3	73.1	16.9	35.1		TH IZZI

GD2314B2	1.5	10	84.93	139.72	4	0.244	0.038	9.3	-0.033	6.4	11.1	0.7	0.9		MW IZZI
GD2314B3	0.9	5	60.1	127.06	4	0.255	0.224	0.7	0.88	14.3	58.8	3.4	1.4		MW IZZI
GD2315B2	3.6	30	82.7	154.31	4	0.430	0.075	5.8	0.159	7.8	13.4	6	5.7		MW IZZI
GD2315B3	1.1	5	84.89	269.1	10	0.496	0.099	4.9	0.338	4	13.3	7.4	13.7		MW IZZI
GD2315B4	2.1	5	102.65	199.11	6	0.364	0.068	6.2	0.131	3.6	11.9	9.2	11.3		MW IZZI
GD2315B5	1	5	119.12	177.42	5	0.241	0.165	1.5	0.036	1.8	6	9.2	2.3	14.7	MW IZZI
GD2316B2	2.5	10	84.22	214.18	6	0.359	0.051	7.7	0.252	3.1	8.6	7.6	12.5		MW IZZI
GD2316B3	1.8	5	105.59	183.84	6	0.284	0.057	6.3	0.211	1.5	4.9	8.1	12.8		MW IZZI
GD2316B4	2.3	5	85.3	176.19	8	0.367	0.085	4.9	0.446	2.9	9	12	10.9		MW IZZI
GD2316B5	1.5	10	100.19	253.89	8	0.427	0.067	7.6	0.273	5.5	6.3	10	14		MW IZZI
GD2316B6	1.3	5	86.41	199.65	9	0.369	0.091	4.2	0.365	1.6	3.4	6.8	9.3		MW IZZI
GD2318B1	0.7	10	0	165.87	9	0.596	0.491	0.1	1.652	13.6	76.7	9	8.5		MW IZZI
GD2318B2	1.7	10	62.16	152.05	5	0.371	0.062	5.9	0.302	4.2	7.8	0.3	0.2		MW IZZI
GD2318B3	1.5	10	85.11	198.07	7	0.669	0.088	5.4	-0.325	10.3	14.3	13.4	15.3		MW IZZI
GD2318B4	2	5	85.3	266.31	10	0.472	0.069	8.5	0.444	2.9	6.2	8	13.8		MW IZZI
GD2318B5	1.6	5	79.31	174.05	6	0.503	0.068	6.7	0.235	5.4	13	13.3	13.2		MW IZZI
GD2318B6	0.6	5	88.48	204.32	7	0.407	0.108	2.9	0.465	5.2	21.8	15.4	10.4		MW IZZI
GD2322B2	1.9	5	101.66	248.07	6	0.492	0.066	8.6	0.3	3.4	6.4	6.1	5.8		MW IZZI
GD2322B3	2.2	10	99.6	247.57	6	0.483	0.135	4.2	0.613	5.7	10.3	15.4	25.1		MW IZZI
GD2322B4	1.4	20	62.95	216.83	7	0.569	0.092	5.0	-0.036	5.4	6.1	8.2	10.1		MW IZZI
GD2315A	3.9	10	0	510	13	0.584	0.288	1.2	1.01	6.7	19.1	3.8	6.3		TH IZZI
GD2322A	1.1	10	240	550	11	0.823	0.220	1.5	1.498	3.6	3	8	5.9		TH IZZI
GD1021B2	0.8	10	106.98	203.59	5	0.522	0.178	2.9	0.106	29.1	48.3	12.2	16.9		MW IZZI
GD1021B3	2.3	10	109.14	155.05	3	0.201	0.105	2.1	0.854	4.8	11.9	0.6	1		MW IZZI
GD1021B4	60.9	10	0	59.97	5	0.401	0.129	1.5	0.002	2.1	12.8	0.8	0.8		MW IZZI
GD1021B5	0.8	5	110.38	156.06	3	0.124	0.148	1.2	0.252	3.5	2.9	0.8	0.4		MW IZZI
GD1021B6	3	15	108.47	144.76	3	0.080	0.254	0.4	1.978	4.8	30.3	0.6	0		MW IZZI
GD1021B7	1.1	10	110.15	132.62	3	0.111	0.158	0.0	-0.539	4	20	50.3	56.3		MW IZZI
GD1072B2	1.9	10	120.62	343.9	6	0.471	0.122	3.7	0.798	14.9	20.5	31.9	24.8		MW IZZI
GD1072B3	1.9	5	107.6	178.5	4	0.205	0.067	3.1	-0.201	4.9	24.7	8.7	4		MW IZZI
GD1072B4	4.4	5	88.38	259.05	7	0.428	0.099	5.6	0.361	9.5	16.5	14.9	29.2		MW IZZI
GD1511B1	9.6	10	44.31	122.97	6	0.492	0.037	16.0	0.051	6.3	6.9	16.6	24.3		MW IZZI
GD1511B2	3.9	10	81.59	136.38	4	0.240	0.014	21.5	-0.073	6.8	6.5	67.5	73.9		MW IZZI

GD1511B3	1.4	5	84.59	168.75	5	0.080	0.242	0.8	1.806	17.2	55.4	64.6	77.6		MW IZZI	
GD1511B4	4.2	5	144.75	287.41	4	0.380	0.044	2.6	0.277	14.7	40.4	61.6	117		MW IZZI	
GD1511B5	7.4	15	44.64	109.34	4	0.409	0.154	2.8	0.481	7.3	14.5	29.7	30.2		MW IZZI	
GD1533B1	3.7	10	44.86	145.44	6	0.565	0.049	9.9	0.253	11.5	22.2	11.3	20.7		MW IZZI	
GD1533B2	14	10	0	113.94	8	0.728	0.070	8.3	-0.2	4.8	5.4	18.7	12		MW IZZI	
GD1533B3	2.7	10	44.33	94.33	4	0.303	0.006	50.8	0.003	6.5	12.3	22.5	10		MW IZZI	
GD1533B4	2.6	5	22.08	54.7	3	0.220	0.158	1.0	1.419	9.1	19.3	62.8	62.8		MW IZZI	
GD1533B5	5.6	15	0	59.91	4	0.381	0.085	2.8	0.384	5.7	13.8	1.1	1.1		MW IZZI	
GD1644B1	1.9	10	68.51	128.34	4	0.237	0.175	1.2	0.455	5.1	22.8	38.2	38.7		MW IZZI	
GD1644B2	1.8	10	22.79	174	8	0.655	0.060	7.5	-0.138	8.8	15.1	22.3	16.5		MW IZZI	
GD1644B3	2.5	10	88.64	199.75	5	0.509	0.071	6.9	0.259	5.9	4.3	13.3	16.8		MW IZZI	
GD1644B4	4.3	5	86.28	278.4	7	0.569	0.078	5.5	-0.263	4.5	5.6	13.9	6.8		MW IZZI	
GD1644B5	2.5	5	43.96	97	7	0.494	0.449	0.4	-0.295	12.5	73.2	10.5	15.1		MW IZZI	
GD1662B3	1.7	10	67.42	131.25	4	0.262	0.138	2.0	0.635	17.4	48.9	13.8	17.3		MW IZZI	
GD1662B4	4.5	10	88.06	138.42	3	0.290	0.251	1.1	-0.179	4	6.1	15	14.4		MW IZZI	
GD1942B2	7.9	30	129.03	293.38	5	0.361	0.106	5.4	0.436	0.4	0.4	65.4	97.5		MW IZZI	
GD1942B3	20	10	133.1	176.13	3	0.183	0.006	27.4	1.474	0.5	2.8	15.3	23.1		MW IZZI	
GD1943B1	26.7	10	81.7	153.65	4	0.461	0.073	3.5	0.394	1.1	2.2	2.9	7		MW IZZI	not used for mean
GD1943B2	13.7	10	86.34	146.22	4	0.373	0.104	2.3	0.913	5.1	11.4	3.8	0.3		MW IZZI	
GD1943B3	3.6	10	134.07	168.52	3	0.088	0.308	0.3	-0.073	2.2	10.4	13.8	2.4		MW IZZI	
GD1943B4	6.1	5	132.08	251.24	4	0.260	0.146	3.3	0.575	3.4	3.2	22.5	9		MW IZZI	
GD1943B5	131.1	15	0	85.83	5	0.391	0.138	1.8	-0.291	0.5	1.4	4	3.5		MW IZZI	
GD1943B6	9.7	10	118.01	203.36	6	0.375	0.159	3.1	0.622	1.2	1.9	23.5	7.7		MW IZZI	
GD37H53B2	3.8	10	86.55	198.31	5	0.225	0.145	2.1	0.664	7.6	22.7	18	21.1		MW IZZI	
GD37H53B3	3.5	10	66.55	108.12	3	0.087	0.280	0.3	1.751	1.7	11	2.5	0		MW IZZI	
GD1021A	10.5	10	280	490	7	0.339	0.167	2.4	0.865	5.9	10.3	4.9	16.2		TH IZZI	
GD1533B	2.4	10	200	460	8	0.456	0.165	3.1	0.606	15	24.1	33.1	22.7		TH IZZI	
GD1651	2.6	10	0	550	15	0.907	0.321	5.8	2.071	21.3	7	20.3	8.9		TH IZZI	
GD1911	2.8	10	240	430	6	0.200	0.235	0.2	-0.906	13.2	83.4	14.2	3		TH IZZI	
GD3753A	18.5	10	100	360	7	0.331	0.094	5.7	0.241	5.1	7.8	8.3	21		TH IZZI	
GD2542B1	2.4	10	22.01	65.72	3	0.272	0.051	1.9	0.513	8.3	34.2	0.4	0.4		MW IZZI	
GD2542B2	1.4	5	21.38	62.51	3	0.301	0.004	28.5	-0.422	9.1	32.6	1.7	1.7		MW IZZI	
GD2562B2	9.9	10	22.05	83.27	4	0.296	0.016	14.2	0.02	3.8	17.5	9	17.4		MW IZZI	

GD2562B3	6.6	10	43.15	171.52	8	0.498	0.145	3.0	0.196	5.1	4	37.5	91.5		MW IZZI
GD2562B4	2.8	15	43.1	200.95	8	0.464	0.135	2.3	-0.065	10.3	41.1	16.9	32.8		MW IZZI
GD2562B5	5	10	0	112.49	6	0.536	0.244	2.1	1.222	3.3	5.7	0.7	1		MW IZZI
GD2562B6	5.4	10	21.59	120.18	6	0.370	0.138	2.4	0.236	2.6	3.9	18.7	41.1		MW IZZI
GD2593B2	12.6	10	63.13	312.04	8	0.738	0.038	19.3	0.041	2.6	2.2	10.4	5.8		MW IZZI
GD2593B3	11.5	15	63.1	130.39	4	0.101	0.138	1.8	0.516	6.8	6.4	60.9	88.2		MW IZZI
GD2593B4	4.6	15	67.35	250.57	6	0.631	0.065	9.1	0.349	6.2	5.7	37.5	38.7		MW IZZI
GD2622B2	9.2	5	71.97	112.57	3	0.234	0.321	0.4	-1.984	14.7	35.9	6.4	11.3		MW IZZI
GD2622B3	2.5	5	40.31	114.68	5	0.511	0.287	0.7	-1.371	36.9	22	24.3	22.3		MW IZZI
GD2632B1	8.4	10	43.03	99.3	5	0.427	0.413	1.0	1.483	15.5	27.8	20.6	25.8		MW IZZI
GD2632B2	1.7	10	41.04	109.38	4	0.431	0.054	7.2	0.088	6.4	11.9	36.8	37.9		MW IZZI
GD2542A	0.9	10	280	550	10	0.810	0.305	0.6	2.264	28.2	26.3	3.9	0.6		TH IZZI
GD2632A	2.2	10	100	400	8	0.473	0.497	0.0	1.625	14.8	62.1	5.6	4.4		TH IZZI
GD2911B2	3.8	10	61.49	143.5	5	0.235	0.050	2.9	0.213	2.1	10.9	5	6.5		MW IZZI
GD2911B3	3.2	5	112.72	191.33	4	0.411	0.047	5.2	0.147	4.6	17.4	26.6	23.9		MW IZZI
GD2911B4	3	5	81.4	155.79	4	0.641	0.031	12.2	0.028	9.9	4.4	1.1	1.9		MW IZZI
GD2913B1	3.3	5	67.04	113.23	5	0.218	0.142	1.5	-0.162	11.1	36.7	34.9	61.7		MW IZZI
GD2913B2	2.3	5	65.25	112.72	5	0.201	0.094	3.9	-0.198	12	29.8	18.6	14		MW IZZI
GD2913B3	2	5	83.22	108.55	6	0.092	0.236	0.1	1.206	2.8	52	88	145.9		MW IZZI
GD2913B4	6.6	5	83.94	146.32	7	0.266	0.143	1.4	0.059	9.7	24.7	15.2	47.1		MW IZZI
GD2913B5	4.7	5	66.05	122.38	5	0.351	0.079	5.1	-0.13	13	10.6	1.9	1.3		MW IZZI
GD2932B2	4.1	10	64.16	134.28	4	0.280	0.115	1.0	0.755	2.5	13.4	3.8	3.5		MW IZZI
GD2932B3	14	10	0	84.64	5	0.266	0.090	1.4	-0.103	4.8	52	13.7	13.3		MW IZZI
GD2932B4	1.8	5	114.75	158.55	5	0.292	0.098	2.6	0.476	2.9	3.1	16.7	29.5		MW IZZI
GD2932B5	2	5	113.71	219.83	7	0.564	0.038	15.9	0.133	4.7	9.6	15.2	37.5		MW IZZI
GD2932B6	2.2	5	115.8	154.7	5	0.324	0.084	2.9	0.301	5.3	19.9	24.8	41.5		MW IZZI
GD2962B2	1.9	5	140.79	223.1	5	0.236	0.064	4.1	0.22	3.3	16.1	22.9	37.4		MW IZZI
GD2981B1	4.6	10	69.23	146.5	4	0.360	0.049	3.1	0.107	0.9	2.7	15.4	13		MW IZZI
GD2981B2	3.3	5	95.19	198.53	7	0.449	0.054	9.2	0.307	2.4	6.3	14.7	17		MW IZZI
GD2981B3	2.1	5	116.22	163.18	5	0.350	0.080	3.9	0.146	4.3	16.2	34.9	44		MW IZZI
GD2981B4	2.6	5	114.37	157.01	5	0.367	0.054	6.9	0.05	4.9	14.4	16.6	24.6		MW IZZI
GD2981B5	2.9	5	116.3	161.47	5	0.400	0.075	4.2	0.15	3.6	12.2	19.2	22.4		MW IZZI
GD2981B6	2.2	5	115.45	237.25	7	0.562	0.087	6.4	0.437	3	6.6	18.9	42.6		MW IZZI

GD2982B2	3.1	5	96.94	190.38	6	0.391	0.079	5.0	0.329	3.7	12.2	8.8	14.9		MW IZZI
GD2992B2	4.3	10	87.24	141.13	3	0.294	0.112	0.6	0.328	3.2	8.9	2.7	0.9		MW IZZI
GD2992B3	3.6	5	85.13	228.51	6	0.440	0.078	5.8	0.412	2.8	5	14.4	20.6		MW IZZI
GD2992B4	3.3	5	111.17	229.6	5	0.366	0.122	3.2	0.422	2.8	7.7	13.6	13.9		MW IZZI
GD29H72B1	10.4	10	101.29	253.37	8	0.384	0.207	1.5	0.405	10.8	42.5	27.6	16.7		MW IZZI
GD29H81B1	4.2	10	0	149.89	11	0.785	0.190	1.6	1.206	22.5	77.2	89.7	53.6		MW IZZI
GD2932A	2.9	10	460	550	4	0.227	0.006	36.9	-0.015	4.5	18.3	3.8	10.1		TH IZZI
GD294B1	0.6	10	430	550	5	0.171	0.623	0.1	0.969	5.2	66.9	4.8	0.4		TH IZZI
GD2962A	7	10	400	550	6	0.293	0.135	2.3	0.445	3.6	16.7	3.2	7.7		TH IZZI
GD2992A	5.6	10	460	550	4	0.172	0.056	2.7	0.079	2.8	18.6	6.9	10.1		TH IZZI

Supplementary table 1: Thellier results and critical SPD values, analysed with paleointensity.org

🟩	specimen passing selection criteria - used for calculation of mean palaeointensity
🟨	critical value fails strict selection criterion but passes relaxed selection criterion
🟥	critical value fails strict and relaxed selection criterion - specimen not used for calculation of mean palaeointensity

Specimen	B anc	Stderr	H lab	AFmin	AFmax	N	FRAC	r2n	r2t	SlopeT	α	MAD a	MAD f
GD0211A	30.2	3.0	5	35	100	14	0.07	0.895	0.987	1.04	2.8	4.5	3.1
GD02HA4	2.2	0.0	10	20	70	8	0.24	0.999	0.998	1.01	6.4	4.9	8.6
GD3381A	15.1	0.5	10	30	70	6	0.28	0.995	0.984	1.12	14.8	7.2	5.3
GD3384B	1.2	0.1	5	40	70	7	0.12	0.982	0.996	0.97	16.3	9.4	8.2
GD14103	0.8	0.1	5	20	70	11	0.14	0.760	0.988	0.93	24.8	20.0	16.9
GD1452A	1.0	0.2	5	20	50	7	0.09	0.784	0.971	0.93	36.2	24.3	30.2
GD2321A	0.9	0.0	5	40	65	6	0.26	0.997	0.999	0.99	10.2	10.0	11.3
GD2341A	1.1	0.0	10	35	75	5	0.31	1.000	1.000	0.93	28.1	7.3	6.1
GD10163	0.7	0.1	10	25	50	5	0.07	0.926	0.999	1.11	1.9	1.0	6.3
GD10202A	0.4	0.0	5	25	60	8	0.61	0.937	0.999	1.03	9.3	29.1	19.8
GD1073A	5.8	1.1	10	2	20	5	0.88	0.900	1.000	1.01	2.0	2.1	1.7
GD1083A	0.3	0.1	5	20	60	9	0.49	0.835	0.989	1.09	35.0	13.4	15.9
GD1541A	0.5	0.1	5	25	50	6	0.47	0.913	0.992	1.03	7.1	13.6	23.2
GD1661A	1.5	0.1	5	30	70	9	0.57	0.975	0.981	1.07	6.5	6.4	6.9
GD1662A	1.5	0.1	5	25	55	7	0.62	0.977	0.991	1.01	12.0	11.8	11.5
GD1942A	23.8	3.8	10	25	50	5	0.02	0.928	0.997	1.05	7.5	6.7	3.1
GD1943A	2.7	0.3	5	25	50	6	0.03	0.944	0.994	0.98	13.3	11.7	4.9
GD3785A	4.2	0.1	5	18	90	17	1.04	0.994	0.999	0.95	0.7	3.3	4.6
GD37H44	7.6	0.3	5	50	90	9	0.38	0.990	0.997	1.05	4.6	1.0	4.5
GD37H53	4.3	0.2	5	27	60	8	0.49	0.993	0.998	1.02	5.8	1.4	4.2
GD2572A	0.8	0.0	10	15	35	5	0.49	0.998	1.000	1.03	4.8	3.3	10.0
GD2582A	0.4	0.1	5	25	55	7	0.23	0.882	0.997	1.03	30.1	13.5	16.0
GD2592A	0.3	0.0	5	25	35	3	0.32	0.999	0.991	0.97	24.8	4.9	13.2
GD2652A	1.0	0.0	5	21	45	7	0.72	0.991	0.999	1.01	5.5	4.9	6.1
GD2662A	1.8	0.1	5	24	65	10	0.68	0.994	0.999	1.01	4.7	4.3	4.5
GD2911A	17.9	0.3	10	30	70	6	0.43	0.999	0.976	0.87	2.6	1.4	1.1
GD2911B	3.5	0.1	5	15	60	12	0.77	0.998	0.999	0.98	0.1	2.1	3.8
GD29141	0.4	0.0	5	18	90	17	0.03	0.892	0.999	0.91	35.1	21.6	32.1
GD291B9	4.6	0.1	10	15	40	6	0.31	0.996	0.999	1.04	2.9	1.5	1.2
GD291B9	5.7	0.2	10	20	100	11	0.23	0.989	0.998	0.99	6.4	4.8	2.1
GD2944A	38.3	1.0	10	15	50	7	0.69	0.997	0.989	0.99	4.2	3.3	1.8
GD2961	3.1	0.1	10	10	50	8	0.92	0.997	0.999	0.95	2.1	1.9	2.2
GD2991	4.2	0.0	10	15	40	6	0.69	1.000	1.000	0.95	2.5	1.6	1.1
GD29H43	-2.5	2.2	10	40	100	7	1.51	0.204	0.201	0.25	15.36	13.2	9.82

Supplementary table 2: Shaw results and critical values.

🟩	specimen passing selection criteria - used for calculation of mean palaeointensity
🟨	critical value fails strict selection criterion but passes relaxed selection criterion
🟥	critical value fails strict and relaxed selection criterion - specimen not used for calculation of mean palaeointensity

Specimen	B anc	H lab	b	σb	AFmin	AFmax	n	B½ARM	f	β	k'	R2	MADFree	α	DANG	k'AA	k'DD	R2 AA
GD0211A	26.9	81.2	-1.089	0.108	35	100	14	18.9	0.186	0.099	0.393	0.885	3.1	0.9	2.8	0.077	0.553	0.928
GD3303	4.0	11.4	-1.13	0.177	15	50	7	7.2	0.243	0.157	0.118	0.881	4.2	4.7	7.5	0.001	0.360	0.924
GD3384B	1.9	81.2	-0.077	0.002	27	50	6	30.9	0.38	0.030	0.144	0.997	4.6	7.9	9.1	-0.004	0.145	0.999
GD0101	0.9	11.4	-0.251	0.021	15	100	12	7.8	0.284	0.083	0.209	0.933	15.3	6.1	12.6	0.004	0.322	0.983
GD14103	0.5	81.2	-0.019	0.004	25	60	8	15	0.246	0.193	-0.032	0.79	21	52.6	65.5	0.043	0.574	0.999
GD1452A	0.7	81.2	-0.029	0.006	20	50	7	10.8	0.238	0.192	-0.315	0.825	30.2	26.8	34.8	0.052	0.466	0.999
GD2321A	1.0	81.2	-0.042	0.002	40	65	6	32.2	0.286	0.046	0.071	0.992	11.3	4.0	5.8	-0.624	1.631	0.606
GD2324	0.5	11.4	-0.145	0.025	40	80	5	30.1	0.246	0.176	-0.781	0.91	18.6	33.3	45.1	-0.034	0.779	1.000
GD1018	1.3	11.4	-0.376	0.017	40	100	7	26.9	0.223	0.044	0.085	0.99	4.6	2.3	4.8	0.153	0.126	0.987
GD10202A	0.8	81.2	-0.031	0.002	30	55	6	29.6	0.311	0.056	0.156	0.987	25.2	28.6	31.5	0.205	0.097	0.995
GD1072A	0.2	81.2	-0.007	0.001	25	40	4	26.7	0.317	0.166	0.974	0.946	19.2	12.4	78.4	-0.022	0.854	1.000
GD1083A	0.5	81.2	-0.02	0.003	30	100	15	27.1	0.406	0.158	-0.44	0.702	25.1	12.0	56.1	0.389	0.741	0.946
GD1542	2.4	11.4	-0.696	0.030	50	100	6	24.9	0.087	0.043	-0.036	0.992	15.2	14.1	21.6	0.047	0.357	0.989
GD1541A	0.5	81.2	-0.019	0.003	25	50	6	27.1	0.294	0.151	-1.044	0.911	23.2	61.9	64.0	-0.158	0.582	1.000
GD1661A	1.3	81.2	-0.054	0.003	30	70	9	26	0.339	0.056	0.087	0.978	6.9	5.6	7.9	0.127	0.058	0.996
GD1662A	1.2	81.2	-0.049	0.003	25	55	7	24.7	0.394	0.070	-0.22	0.975	11.5	7.1	8.5	0.149	0.295	0.996
GD1943A	3.2	81.2	-0.129	0.015	25	50	6	24.3	0.376	0.118	0.632	0.945	4.9	10.0	15.4	-1.147	0.982	0.446
GD3785A	3.1	81.2	-0.125	0.002	21	95	17	19.6	0.446	0.020	-0.165	0.994	4.2	2.0	4.3	0.051	0.236	0.998
GD37H44	11.2	81.2	-0.454	0.026	50	90	9	26.2	0.197	0.057	-0.136	0.978	4.5	2.9	3.6	-2.195	1.935	0.355
GD37H53	6.1	81.2	-0.245	0.009	27	60	8	22.7	0.271	0.038	-0.119	0.991	4.2	20.0	22.3	0.002	0.103	0.997
GD2582A	0.3	81.2	-0.011	0.002	27	55	7	24.2	0.326	0.150	0.547	0.891	16	39.7	47.2	0.093	0.449	0.998
GD2592A	0.2	81.2	-0.009	0.002	24	40	5	26	0.185	0.201	-0.592	0.883	20.9	55.8	56.6	0.114	0.479	0.999
GD2652A	0.9	81.2	-0.035	0.002	21	45	7	24.9	0.483	0.049	-0.259	0.988	6.1	3.0	3.6	0.064	0.290	0.999
GD2662A	1.5	81.2	-0.061	0.002	24	65	10	22.7	0.418	0.031	-0.201	0.992	4.5	4.5	6.7	0.030	0.227	1.000
GD2911B	2.7	81.2	-0.11	0.008	35	75	9	23.9	0.234	0.068	-0.081	0.968	4.8	4.7	6.2	0.073	0.122	0.995
GD2913	4.1	81.2	-1.17	0.033	10	40	7	29	0.669	0.028	-0.042	0.996	1.6	1.3	1.6	-0.116	0.084	0.995
GD29141	0.3	81.2	-0.013	0.001	18	95	18	20.8	0.548	0.090	0.381	0.876	31.3	5.5	6.3	0.146	0.346	0.993
GD294B1A	6.5	81.2	-0.264	0.031	0	15	6	18.6	0.767	0.116	0.686	0.947	8.4	15.0	18.4	0.104	0.770	0.997

Supplementary table 3: Pseudo-Thellier results and critical values, analysed with paleointensity.org

🟩	specimen passing selection criteria - used for calculation of mean palaeointensity
🟨	critical value fails strict selection criterion but passes relaxed selection criterion
🟥	critical value fails strict and relaxed selection criterion - specimen not used for calculation of mean palaeointensity

		A Selcrit2 mod			A MC-crit.C1			A Picrit03			A TTA			A+B Selcrit2 mod			A+B Shaw			A Shaw		
Site	N	N	PI	Std	N	PI	Std	N	PI	Std	N	PI	Std	N	PI	Std	N	PI	Std	N	PI	Std
GD02	11	1	2.1		0			2	2.2	0.05	1	1.8		1	2.1		1	2.18		1	2.18	
GD33	16	3	2.6	0.6	1	3.5		4	2.5	0.58	5	2.5	0.59	5	2.6	0.62	0			0		
GD01	4	0			0			0			0			0			0			0		
GD14	3	0			0			0			0			1	7.6		0			0		
GD23	23	5	2.0	0.84	9	1.9	0.37	6	1.7	0.37	5	1.7	0.33	12	1.9	0.67	1	0.92		1	0.92	
GD10	11	0			0			0			0			0			0			0		
GD15	11	1	5.6		0			0			0			1	5.6		0			0		
GD16	8	0			0			0			0			1	4.3		0			0		
GD19	10	0			0			0			0			0			0			0		
GD37	3	0			0			0			0			0			3	5.3	1.6	0		
GD29	38	2	3.9	0.85	3	6.8	6.27	6	5.2	4.05	0			3	3.6	0.78	4	3.8	0.58	4	3.8	0.58
GD07	1	0			0			0			0			0			0			0		
GD25	12	1	12.6		0			1	13.3		1	12.3		1	12.6		1	0.76		1	0.76	
GD26	5	0			0			0			0			0			2	1.37	0.4	0		
GD30	1	0			0			0			0			0			0			0		
All	157	13	4.8	3.7	13	4.0	2.0	19	5.0	4.3	12	4.6	4.5	25	5.0	3.4	12	2.4	1.7	7	1.9	1.2

Supplementary table 4: Comparison of different sets of selection criteria: Site/Dyke name, total number of experiments, result class and used set of criteria, number of accepted results, intensity (µT), standard deviation. blue fields show average values for the locality. Results are analysed and compared with strict selection criteria from modified SELCRIT2 (Biggin et al., 2007), MC-crit.C1 (Paterson et al., 2015), PICRIT03 (Kissel and Laj, 2004) and TTA (Leonhardt et al., 2004). The results of Thelllier type experiments in this study, including class B results are shown with the results of the Shaw experiments as comparison. The similarity of results shows a high consistency between the different methods and that there is no significant bias connected to the choice of selection criteria.

Unit	AGE	STAT	TRM	ALT	MD	ACN	TECH	LITH	MAG	QPI
GD02	1	0	1	1	1	1	1	0	1	7
GD33	1	1	1	1	1	1	0	0	1	7
GD14	1	0	1	1	1	1	0	0	1	6
GD23	1	0	1	1	1	1	1	0	1	7
GD15	1	0	1	1	1	1	0	0	1	6
GD16	1	0	1	1	1	1	0	0	1	6
GD37	1	0	1	1	1	1	0	1	1	7
GD29	1	1	1	1	1	1	1	0	1	8
GD25	1	0	1	1	1	1	1	0	1	7
GD26	1	0	1	1	1	1	0	0	1	6

Supplementary table 5: List of QPI criteria (Paterson et al., 2014) for all sites yielding palaeointensity results.

For details, the readers are referred to section 4 of the main text.